



Effects of Thermodynamics, Dynamics and Aerosols on Cirrus Clouds Based on In Situ Observations and NCAR CAM6 Model

Ryan Patnaude¹, Minghui Diao¹, Xiaohong Liu², Suqian Chu³

¹Department of Meteorology and Climate Science, San Jose State University, San Jose, 95192, USA

²Department of Atmospheric Sciences, Texas A&M University, College Station, 77843, USA,

³Department of Atmospheric Science, University of Wyoming, Laramie, 82071, USA

Correspondence to: Minghui Diao (minghui.diao@sjsu.edu)

Abstract. Cirrus cloud radiative effects are largely affected by ice microphysical properties, including ice water content (IWC), ice crystal number concentration (Ni) and mean diameter (Di). These characteristics vary significantly due to 10 thermodynamic, dynamical and aerosol conditions. In this work, a global-scale observation dataset is used to examine regional variations of cirrus cloud microphysical properties, as well as several key controlling factors, i.e., temperature, relative humidity with respect to ice (RHi), vertical velocity (w), and aerosol number concentrations (Na). Results are compared with simulations from the National Center for Atmospheric Research (NCAR) Community Atmosphere Model version 6 (CAM6). The differences between simulations and observations are found to vary with latitude and temperature. 15 Specifically, simulations are found to underestimate IWC by a factor of 5–30 in all regions. Simulated Ni is overestimated in most regions except Northern Hemisphere midlatitude and polar regions. Simulated Di is underestimated, especially for warmer conditions (-50°C to -40°C) and higher Na, possibly due to less effective ice particle growth/sedimentation and weaker aerosol indirect effects, respectively. For RHi effects, the frequency and magnitude of ice supersaturation is underestimated in simulations for clear-sky conditions, and the simulated IWC and Ni show maximum values at 80% RHi 20 instead of 110% as observed. For w effects, both observations and simulations show variances of w (σ_w) decreasing from tropics to polar regions, but simulations show much higher σ_w for in-cloud condition than clear-sky condition. These findings provide an observation-based guideline for improving simulated ice microphysical properties and their relationships with key controlling factors at various geographical locations.

1 Introduction

25 Cirrus clouds represent one of the most ubiquitous cloud types with an estimated global coverage of approximately 20% to 40% (Mace and Wrenn, 2013; Sassen et al., 2008). According to the fifth assessment of the United Nations Intergovernmental Panel on Climate Change (IPCC) report (Boucher et al., 2013), the largest uncertainty in estimating future climate change stems from clouds and aerosols. Unlike most other cloud types, cirrus clouds may produce a net positive or negative radiative forcing depending on their microphysical properties (Stephens and Webster, 1981; Zhang et al., 1999), 30 which are affected by meteorological conditions and aerosol distributions. Tan et al. (2016) showed that the radiative effects



of misrepresenting the prerequisite condition of cirrus clouds – ice supersaturation (ISS, where relative humidity with respect to ice (RHi) $> 100\%$) – can lead to an average bias of $+2.49 \text{ W/m}^2$ at the top of the atmosphere. Other modelling studies found large differences in the net cloud radiative forcing depending on the fraction of activated ice nucleating particles (INPs) and the nucleation mechanisms (i.e., homogeneous and heterogeneous nucleation) through which the clouds form

35 (Liu et al., 2012; Storelvmo and Herger, 2014). The large uncertainties in cirrus cloud radiative forcing illustrate the need for further study on cirrus cloud microphysical properties as well as their controlling factors in various geographical locations.

Ideally, a comprehensive quantification of cirrus cloud microphysical properties globally based on high-resolution, in situ observations would mitigate many uncertainties. However, challenges remain in field measurements to achieve such spatial coverage. Previously, efforts have been made to understand cirrus cloud properties based on their geographical locations.

40 Diao et al. (2014b) performed a hemispheric comparison of in situ cirrus evolution and found little difference in the clear-sky ISS frequency as well as the proportion of each evolution phase between the Northern and Southern Hemispheres (NH and SH, respectively). Another study investigated the ice water content (IWC) and snowfall rates for tropical, midlatitude, and Arctic cirrus clouds using in situ observations and found a geographical dependence of IWC (Heymsfield et al., 2017). Wolf et al. (2018) used balloon-based in situ observations to analyze microphysical properties of Arctic ice clouds and found 45 differences in particle size distributions (PSDs) depending on the cloud origin. Krämer et al. (2016, 2020) developed a cirrus cloud climatology, focusing on tropical and midlatitude cirrus clouds, and showed that cloud thickness is larger at lower altitudes, and thus producing a more negative radiative forcing. Moving from north to south using lidar-based observations from two research cruises starting from Leipzig, Germany, one to Punta Arenas, Chile and the other one to Stellenbosch, South Africa, Kanitz et al. (2011) observed a decrease in the efficiency of heterogeneous nucleation in the SH, which could 50 be a result of fewer INPs. This hemispheric difference in aerosol indirect effects is consistent with significantly higher aerosol number concentrations in the NH (Minikin et al., 2003).

Regional and hemispheric variations of cirrus microphysical properties are produced by various controlling factors, such as thermodynamics (i.e., temperature and RHi), dynamics (e.g., vertical velocity) and aerosols (e.g., number concentration and composition). The effects of temperature have been extensively studied from in situ observations (Heymsfield et al., 2017; 55 Luebke et al., 2013, 2016; Schiller et al., 2008), showing an increase of IWC towards warmer temperatures. A number of studies focused on distributions of RHi have found that in-cloud RHi occurs most frequently at or near 100% (Jensen et al., 2001; Krämer et al., 2009). Another study by Diao et al. (2017) found that using different RHi thresholds (e.g., 108% to 130%) for ice nucleation in simulations can influence IWC and ice crystal number concentrations (Ni) in convective cirrus. In addition, the spatial scales of ice supersaturated regions can vary from the micro- to mesoscales, largely depending on the 60 spatial variability of water vapor (Diao et al., 2014a). The distributions of vertical velocity have been investigated in different types of cirrus clouds, such as in ridge-crest cirrus, frontal cirrus and anvil cirrus (Muhlbauer et al., 2014a, 2014b). Stronger updrafts are found to be associated with higher occurrence frequency of ISS inside anvil and convective cirrus (D'Alessandro et al., 2017). Regarding the effects of aerosols, Cziczo et al. (2013) and Cziczo and Froyd (2014) investigated ice crystal residuals from in situ observations and discovered that the majority of midlatitude cirrus clouds form via



65 heterogeneous nucleation on mineral dust and metallic particles. Anthropogenic aerosols, such as secondary organic aerosols, were found to be less effective INPs compared with mineral dust (Prenni et al., 2009). Based on remote sensing data, Zhao et al. (2018, 2019) showed that the correlations between ice crystal sizes and aerosol optical depth can be either positive or negative depending on the meteorological conditions in convective clouds. Chylek et al. (2006) showed an increase in ice crystal size during the more polluted winter months compared with cleaner summer months over the eastern
70 Indian Ocean. Using a global-scale dataset of multiple flight campaigns, Patnaude and Diao (2020) isolated individual effects on cirrus clouds from temperature, RH_i, vertical velocity (w) and aerosol number concentrations (Na). They found that when Na is 3 – 10 times higher than average conditions, it shows strong positive correlations with cirrus microphysical properties such as IWC, Ni and number-weighted mean diameter (Di). These aerosol indirect effects are also susceptible to whether or not thermodynamic and dynamical conditions are controlled, demonstrating the importance of conducting a
75 comprehensive analysis of various key controlling factors altogether.

More recently, in situ observations have been used to evaluate and improve cirrus cloud parameterizations in global climate models (GCMs). Two types of simulations have been frequently used for model evaluation, i.e., free-running (Eidhammer et al., 2014, 2017; Wang and Penner, 2010; Zhang et al., 2013) and nudged (D'Alessandro et al., 2019; Kooperman et al., 2012; Wu et al., 2017) simulations. For free-running simulations, a comparison on statistical distributions of ice microphysical properties is often used for model validation (e.g., Penner et al., 2009). The nudged simulation would nudge certain meteorological conditions towards reanalysis data, such as horizontal wind and temperature (e.g., D'Alessandro et al., 2019; Wu et al., 2017). These nudged simulations can also be output to similar location and time as those of the aircraft observations. Given the importance and limited understanding of how aerosols interact with cirrus clouds, much attention has been dedicated to the parameterization of aerosol indirect effects (Kärcher and Lohmann, 2002, 2003; Kuebbeler et al.,
85 2014; Wang et al., 2014). Shi et al. (2015) added the effects of pre-existing ice into the Community Atmosphere Model Version 5 (CAM5) and found a decrease in Ni due to the reduction of homogeneous nucleation frequency. Other studies also investigated the effect of updraft velocity on simulated Ni and aerosol indirect effects (Zhou et al., 2016; Penner et al., 2018).

This study aims to bridge the knowledge gap on how cirrus clouds vary depending on geographical locations and
90 environmental conditions by using a comprehensive in situ observation dataset that includes seven U.S. National Science Foundation (NSF) flight campaigns. Observations were collected onboard the NSF/National Center for Atmospheric Research (NCAR) Gulfstream-V (G-V) research aircraft. Descriptions of the seven flight campaigns, instrumentations, model configurations of the NCAR Community Atmosphere Model version 6 (CAM6) are provided in Section 2. Both observations and simulations are used to examine the regional variations in the statistical distributions of cirrus
95 microphysical properties, including IWC, Ni and Di (Section 3). Impacts of several key controlling factors, i.e., temperature, RH_i, w and Na, are examined in Section 4. Discussions on observation-based findings and model evaluation results are included in Section 5.



2 Data and Methods

2.1 In situ observations and instrumentations

100 In this study, in situ airborne observations at 1 Hz are provided by instruments onboard the NSF High-Performance
Instrumented Airborne Platform for Environmental Research (HIAPER) G-V research aircraft. A comprehensive global
dataset is compiled based on seven major flight campaigns funded by the NSF, including START08 (Pan et al., 2010),
HIPPO deployments 2–5 (Wofsy et al., 2011), PREDICT (Montgomery et al., 2012), TORERO (Volkamer et al., 2015),
DC3 (Barth et al., 2015), CONTRAST (Pan et al., 2017), and ORCAS (Stephens et al., 2018). Table 1 provides a detailed
105 summary of the seven flight campaigns, including location, duration of flights, total flight hours of all temperatures, and
flight hours for in-cloud and clear-sky conditions at temperatures $\leq -40^{\circ}\text{C}$ only. Maps comparing the flight tracks of in situ
observations and collocated CAM6-nudg data are shown in Figure 1.

For this study, ice particle measurements are provided by the Fast 2-Dimensional Cloud particle imaging probe (Fast-2DC)
with a 64-diode laser array for a range of 25 μm – 1600 μm . Larger particles can be reconstructed up to 3200 μm . The mass-
110 Dimensional relationship of Brown and Francis (1995) is used to calculate IWC for the Fast-2DC probe, which was
previously used in other studies of the Fast-2DC probe onboard the NSF G-V aircraft (Diao et al., 2014a, 2014b, 2015).
Number-weighted mean diameter (Di) is calculated by summing up the size of particles in each bin using the bin center, and
then dividing it by the total number of particles. In order to mitigate the shattering effect, particles $< 62.5 \mu\text{m}$ (i.e., first two
bins) are excluded in the Fast-2DC measurements when calculating IWC, Ni and Di . The Rosemount temperature probe was
115 used for temperature measurements, which has an accuracy and precision of $\sim \pm 0.3 \text{ K}$ and 0.01 K, respectively. All analyses
are restricted to temperatures $\leq -40^{\circ}\text{C}$, in order to exclude the presence of supercooled liquid droplets in this study.
Laboratory calibrated and quality-controlled water vapor data were collected using the Vertical Cavity Surface Emitting
Laser (VCSEL) hygrometer (Zondlo et al., 2010), with an accuracy of $\sim 6\%$ and precision of $\leq 1\%$. Both temperature and
water vapor are used at 1-Hz resolution for this analysis. Aerosol measurements were collected from the Ultra-High
120 Sensitivity Aerosol Spectrometer (UHSAS), which uses 100 logarithmically spaced bins ranging from 0.06 – 1 μm . RHi is
calculated using saturation vapor pressure with respect to ice from Murphy and Koop (2005). The combined RHi
uncertainties from the measurements of temperature and water vapor range from 6.9% at -40°C to 7.8% at -78°C .
Measurements are separated by cloud condition whereas in-cloud condition is defined by the presence of at least one ice
crystal from the Fast 2-DC probe ($\text{Ni} > 0 \text{ L}^{-1}$). The same in-cloud definition has been used by several previous studies
125 (D'Alessandro et al., 2017; Diao et al., 2014a, 2014b, 2015, 2017; Tan et al., 2016), and all other samples are defined as
clear sky. For regional variation analysis, data are binned by six latitudinal regions in the two hemispheres, that is, NH polar
(60°N – 90°N), SH polar (60°S – 90°S), NH midlatitude (30°N – 60°N), SH midlatitude (30°S – 60°S), NH tropics (0° –
30°N), and SH tropics (0° – 30°S).

130 The vertical profiles of observed in-cloud temperature, clear-sky potential temperature (Θ), and their correlations are shown
in Figure 2. The observations sampled temperatures from -78°C to -40°C and altitudes from 5 – 15 km, while a previous



study of Krämer et al. (2020) sampled -91°C to -30°C and 5 – 19 km (their Figure 2). The lowest temperatures are found in the tropical regions and at the highest altitudes, whereas polar regions show more observations at lower altitudes that satisfy temperature $\leq -40^\circ\text{C}$. Distributions of cirrus cloud properties (i.e., IWC, Ni, Di), in-cloud and clear-sky RH_i, and clear-sky water vapor mixing ratio for the observation dataset are shown in Figure 3. Di increases with decreasing altitudes, IWC 135 slightly increases with decreasing altitudes, and Ni is almost independent of altitudes. Clear-sky RH_i and water vapor mixing ratio both increase with decreasing altitudes, while in-cloud RH_i is centered around 100% and shows smaller dependency on altitudes. Compared with Figure 3 in Krämer et al. (2020), 48% of their ice particle samples have Di < 40 μm , which is 140 below the size cut-off used in this study. The higher Di in this study also leads to lower range of Ni (0.01 – 1000 L^{-1}) and higher range of IWC (10^{-5} – 10 g m^{-3}) compared with that previous study (i.e., Ni from 0.1 – 10^5 L^{-1} and IWC from 10^{-7} – 1 g m^{-3}).

2.2 Climate model description and experiment design

This study uses model simulations based on the NCAR CAM6 model. Compared with its previous version – the CAM5 model, CAM6 implemented a new scheme, the Clouds Layers Unified by Binomials (CLUBB) for representations of boundary layer turbulence, shallow convection and cloud macrophysics (Bogenschutz et al., 2013). CLUBB is a higher-order 145 turbulence closure scheme that calculates prognostic higher-moments based on joint probability density function (PDFs) for vertical velocity, temperature, and moisture (Golaz et al., 2002). An improved bulk two-moment cloud microphysics scheme has been implemented (Gettelman and Morrison, 2015) that replaces diagnostic treatment of rain and snow with prognostic treatment of all hydrometeors (i.e., rain, snow, graupel, hail). This is coupled with a 4-mode aerosol model (MAM4) (Liu et al., 2016) for simulations of aerosols and aerosol-cloud interactions. It allows ice crystals to form via homogeneous freezing 150 of sulfate aerosols and heterogeneous nucleation of dust particles (Liu et al., 2007; Liu and Penner, 2005). Finally, the deep convection scheme (Zhang and McFarlane, 1995) has been tuned to include sensitivity to convection inhibition.

Results from in situ observations are compared with two types of CAM6 simulations, nudged and free-running simulations. Simulations are based on a finite-volume dynamical core (Lin, 2004) with a horizontal resolution of $0.9^\circ \times 1.25^\circ$ and 32 vertical levels. All simulations are conducted using prescribed sea-surface temperature and present-day aerosol emissions 155 and include a 6-month spin-up time. CAM6 nudged simulations are nudged spatially and temporally with meteorological data (i.e., 2-D horizontal wind and temperature) from the Modern-Era Retrospective Analysis for Research and Applications version 2 (MERRA2) (Gelaro et al., 2017), and collocated with aircraft flight tracks in space and time. A nudged simulation was conducted for each campaign independently and was combined into one data set (hereafter named “CAM6-nudg”) to compare with observations. One free-running simulation was conducted for the duration of all flight campaigns from July 160 2008 to February 2016. To reduce the size of model output when comparing with observations, a total of 24 instantaneous output from the free-running simulation are combined into one data set (“CAM6-free” hereafter), which includes 00 and 12 UTC for the first day of each month in 2010. Additional sensitivity tests on different model output from the free-running



simulation show very minor differences in the statistical distributions of cirrus microphysical properties and the correlations with their controlling factors when selecting different years, seasons, and days in a month.

165 In-cloud conditions in simulations are defined by concurring conditions of $IWC > 10^{-5} \text{ g m}^{-3}$ and $Ni > 10^{-2} \text{ L}^{-1}$, which are the lower limits from observations. In addition, analysis of simulated cirrus clouds is restricted to similar pressure ranges as those measured in the seven campaigns. An additional constraint on cloud fraction $> 10^{-5}$ was applied to CAM6-free to exclude extremely low values. A summary of the ranges of meteorological conditions and ice microphysical properties for in situ and simulation data is shown in Table 2. Simulated ice and snow are restricted to $> 62.5 \mu\text{m}$ based on the size cut-off of
170 the Fast-2DC probe. Note that due to the ice crystal size constraint, some thin cirrus may not be detected. IWC , Ni and Di values are re-calculated by combining snow and ice for their mass and number concentrations based on a similar method from Eidhammer et al. (2014), which also combined snow and ice to compare with in situ data. In addition, simulated aerosols number concentrations are further categorized by diameters $> 500 \text{ nm}$ and $> 100 \text{ nm}$ (i.e., Na_{500} and Na_{100} , respectively), by summing the size-restricted concentrations of the Aitken, accumulation and coarse aerosol modes.
175 Previously, field experiments found that Na_{500} correlates well with INP number concentrations (DeMott et al., 2010). Even though that correlation was only determined based on observations warmer than -36°C , the separation of Na_{500} and Na_{100} can help to examine the effects of larger and smaller aerosols in this work.

3 Regional variations of cirrus cloud characteristics

3.1 Cirrus cloud microphysical properties with respect to temperature

180 Three cirrus cloud microphysical properties, IWC , Ni and Di are examined in relation to temperature at six latitudinal regions (Figure 4). The observations of IWC and Ni in the NH indicate clear latitudinal differences with the highest values occurring in the midlatitudes, followed by tropics, then polar regions for temperatures between -40°C and -60°C , while for colder temperatures the NH tropical region shows the highest IWC . In the SH, the highest IWC and Ni occur in the tropics, followed by the polar regions and midlatitudes. Comparing the two hemispheres, IWC and Ni show significant reductions by
185 ~ 1 order of magnitude from NH midlatitude to SH midlatitude (Figure 5). The IWC , Ni and Di are relatively similar between NH and SH tropical regions, while IWC and Di are higher in the SH polar region than NH polar regions.
CAM6-nudg data show similar trend of average IWC , Ni and Di with respect to temperature as seen in observations, that is, the average IWC increases with increasing temperature consistent with previous observational studies (Krämer et al., 2016; Luebke et al., 2013; Schiller et al., 2008), average Ni shows no clear trend with temperature, and average Di increases with
190 increasing temperature. Differing from observations, CAM6 produces the highest IWC and Ni in the tropical regions, followed by midlatitudes then polar regions for both hemispheres. The simulated Di also shows little difference between hemispheres and latitudes. Overall, the major problem of the simulation is the underestimation of average IWC by a factor of 2 – 10, which leads to the underestimation of average Di by a factor of 1.2 – 2. The comparison of Ni shows relatively better results, with the simulated average Ni being higher than observations in the tropics at -55°C to -40°C and in SH extratropical



195 regions, but lower than observations in the NH midlatitude. This result indicates “too many” and “too small” simulated ice in most regions, except for “too few” and “too small” simulated ice in the NH midlatitude. The larger differences in average Di occur in the temperatures closer to -40°C , which indicates possible misrepresentation of ice particle growth and sedimentation into the relatively warmer regions in the model parameterization.

200 A previous study by Righi et al. (2020) evaluated the ice microphysical properties in EMAC-MADE3 aerosol–climate model (i.e., ECHAM/MESSy Atmospheric Chemistry-Modal Aerosol Dynamics model for Europe adapted for global applications, 3rd generation) by comparing with in situ observations of multiple aircraft field campaigns from 75°N to 25°S (Krämer et al., 2009, 2016, 2020). That study showed low biases of simulated Di at $190 - 243\text{ K}$, low biases of simulated IWC at $205 - 235\text{ K}$, as well as high biases of simulated Ni above 225 K , which are generally in the same direction as the biases we found in CAM6 model. Note that Righi et al. (2020) implemented different cloud microphysics parameterizations compared with the 205 CAM6 model, including a two-moment cloud microphysics scheme of Kuebbeler et al. (2014) and the ice nucleation parameterization for cirrus clouds ($T < 238.15\text{ K}$) from Kärcher et al. (2006) which account for both homogeneous and heterogeneous nucleation and the competition between the two mechanisms. More future intercomparison studies of these models are warranted to examine the reasons behind the similar biases.

3.2 RHi and σ_w distributions for in-cloud and clear-sky conditions

210 Regional distributions of RHi for clear-sky and in-cloud conditions are shown for observations (Figure 6) and simulations (Figure 7). Observations show RHi magnitudes ranging from $< 5\%$ up to $\sim 180\%$ in both clear-sky and in-cloud conditions, and mostly locate below the homogeneous freezing line except for the NH tropical region. A few samples exceed liquid 215 saturation line but are within the measurement uncertainties of RHi. This result agrees with the RHi distributions based on previous midlatitudinal observations (Cziczo et al., 2013). For clear-sky conditions, the majority of the observed and simulated RHi values are below 100%, while the CAM6-nudg data show fewer RHi exceeding ice saturation. For in-cloud conditions, both observations and simulations show that RHi frequently occur within $\sim 20\%$ of ice saturation, consistent with previous observation and modeling studies (Diao et al., 2014a, 2017; D’Alessandro et al., 2017, 2019; Krämer et al., 2009), while almost no simulated RHi data exceed the homogeneous freezing threshold. The higher RHi observed in the NH 220 tropical region was also observed by Krämer et al. (2009). Such feature can be explained by the competition between higher updrafts seen in the tropics and the depletion of water vapor from newly nucleated ice particles as discussed in Kärcher and Lohmann (2002). For the polar regions, in-cloud RHi is skewed towards ISS in both observations and simulations, indicating less effective water vapor depletion likely due to lower Ni values (Figure 5 f).

225 Regional distributions of the variance of w (σ_w) for in situ observations and CAM6 nudged simulations are shown in Figures 8 and 9, respectively. σ_w in the observations is calculated as the variance of w within each 200 seconds of data, which corresponds to a horizontal scale of $\sim 46\text{ km}$, similar to the horizontal grid scale of the CAM6 simulations. The σ_w in simulations is based on the “wsub” variable, which is calculated from the square root of turbulent kinetic energy (TKE) (Gettelman et al., 2010). Observed σ_w shows the highest values in the tropical and midlatitude regions reaching up to $\sim 3\text{ m/s}$,



while the polar regions show updrafts up to ~ 1 m/s. A similar decreasing trend of maximum σ_w is seen in the simulations from the lower to higher latitudes. The observations show similar σ_w maximum values between clear-sky and in-cloud 230 conditions, while the simulations show much higher maximum σ_w for in-cloud conditions in the tropics (1 m/s), midlatitude (1 m/s) and polar regions (0.5 m/s), compared with those values in clear sky (i.e., 0.25, 0.25 and 0.1 m/s, respectively). This result suggests that the model has a stronger dependence on higher σ_w for cirrus cloud formation compared with observations.

4 Individual impacts of key controlling factors on cirrus clouds

235 4.1 Probability density functions of temperature, RHi and σ_w

PDFs of temperature, RHi and σ_w are shown in Figure 10. The PDFs are normalized by the total number of samples of both clear-sky and in-cloud conditions. The observations are located mostly around -68°C to -40°C , and the simulations show similar temperature distributions. For the PDFs of RHi, the observations and simulations all show peak position at 100% for in-cloud condition. However, a secondary peak is shown in simulations at 80% RHi, which is likely due to the parameter of 240 RH_{min} for ice cloud fraction calculation being set at 80% for representing variance of humidity in a grid box (more details on RH_{min} are described in Gettelman et al. (2010)). In addition, the maximum RHi values are 170% and 180% for in-cloud and clear-sky conditions in the observations, while the CAM-nudg simulations show lower values at 160% and 150%, respectively. The CAM-free data show higher maximum RHi values than CAM-nudg data, likely due to additional data from 245 tropical regions at temperatures below -70°C (Figure 10 c). When using a lower size cut-off (1 μm) of ice particles for the simulation data, the number of in-cloud samples increases (supplementary Figure S1). However, negligible differences are seen in the PDFs of temperature, RHi and σ_w for the two simulations between Figures 10 and S1. Specifically, the steeper decrease of probability for $\text{RHi} > 100\%$ is consistently shown in the simulations regardless of the ice particle size range. PDFs of σ_w show consistent results to Figures 8 and 9, with simulations showing much higher maximum σ_w for in-cloud 250 conditions than clear-sky conditions compared with the observations. The lower maximum values of σ_w in simulations are most likely a result of model missing representations of gravity waves from topography, fronts, and convection, and only including σ_w from turbulence.

4.2 Effects of RHi and σ_w on ice microphysics

The relationships between ice microphysical properties and RHi are examined in Figure 11. For the observations, the maximum IWC and Ni occur slightly above ice saturation at 110% RHi, while the maximum Di occur at 130% RHi. The 255 average IWC and Ni increase 1.5 orders of magnitude from 40% to 110% RHi, and decreases 0.5 order of magnitude (i.e., a factor of 3) from 110% to 130% RHi. The maximum IWC and Ni do not occur at the highest RHi most likely due to the consumption of water vapor by ice deposition. High Di values at lower RHi ($\sim 30\%$) are likely a result of sedimenting large



ice crystals, which has been previously observed by Diao et al. (2013) when investigating the evolutionary phases of cirrus clouds.

260 In contrast to observations, both CAM6-nudg and CAM6-free simulations show a primary peak of average IWC and Ni at 80% RHi and a secondary peak at 100% RHi, with a local minimum at 90% RHi. The peak at RHi 80% is likely produced by the RH_{min} parameter reflecting sub-grid scale RHi variance as mentioned above (Gettelman et al., 2010). Smaller increases in IWC and Ni are shown in the simulations (i.e., 0.5 order of magnitude) compared with observations as RHi increases from 40% to 100%. Increases of average IWC and Ni are seen in the simulations as RHi increases from 110% to 140%, differing 265 from the decreasing trend seen in the observations. The simulations may underestimate water vapor depletion rate since the average IWC and Ni in the simulations are lower than the observations by 0.5 order of magnitude at 110% – 140% RHi. For Di - RHi correlations, both simulations show similar results to the observations, with the maximum Di around 130% RHi and some large ice particles in the subsaturated conditions. The large variability of observed ice microphysical properties is also significantly underestimated in the model for ISS conditions. Standard deviations are 0.5 – 1 order of magnitude lower 270 for IWC and Ni and a factor of 2 lower for Di compared with observations.

Comparing the correlations with σ_w (Figure 12), the simulations show increasing IWC and Ni with higher σ_w , which agree with observations. The simulated Di is relatively constant with increasing σ_w , which differs from the observed positive correlation between Di and σ_w . This positive Di - σ_w correlation is likely due to the growth of ice particles as cirrus clouds 275 evolve with continuous updrafts that supply excess water vapor above ice saturation, which was previously discussed in a cirrus cloud evolution analysis (Diao et al., 2013). The simulations may overlook this positive correlation due to several reasons, such as the lack of temporal resolution to resolve cirrus evolution in the growth phase, the lack of vertical velocity sub-grid variabilities (as discussed in Zhou et al. (2016)), and a dry bias (i.e., lower RHi) in the model (as discussed in Wu et al. (2017)).

4.3 Aerosol indirect effects

280 The effects of larger and smaller aerosols (i.e., Na_{500} and Na_{100}) on ice microphysical properties are further examined for observations and CAM6-nudg data (Figure 13). Cloud fraction is calculated in each temperature – Na bin by normalizing the number of in-cloud samples with the total number of samples in that bin. For three cirrus microphysical properties (i.e., IWC, Ni and Di), positive correlations are seen in observations with respect to Na_{500} and Na_{100} . In addition, higher Na_{500} ($>10 \text{ cm}^{-3}$) and Na_{100} ($>100 \text{ cm}^{-3}$) values are associated with significant increases in cloud fraction. At -70°C to -60°C , higher 285 IWC, Ni and cloud fraction are seen when Na_{500} is observed, with positive correlations of IWC and Ni with respect to Na_{500} . This finding indicates that larger aerosols provide an effective pathway of ice particle formation for colder conditions. The higher IWC and Ni are only shown in much higher Na_{100} ($>100 \text{ cm}^{-3}$) between -70°C and -60°C , demonstrating that larger aerosols facilitate ice formation more effectively than smaller aerosols at this temperature range, possibly due to the activation of larger aerosols as INPs for heterogeneous nucleation.



290 The CAM6-nudg simulation shows increasing average IWC, average Ni and cloud fraction with increasing Na_{500} , consistent
with the observations. But at temperatures below $-60^{\circ}C$, simulated IWC and Ni do not show a sudden increase when Na_{500}
exists as shown in the observations. The simulated Di slightly decreases with increasing Na_{500} , differing from the increasing
trend seen in observations. For aerosol indirect effect analysis based on Na_{100} , the comparison results are similar to Na_{500} ,
that is, CAM-nudg simulation is able to represent positive correlations of Ni and cloud fraction with respect to Na_{100} , but
295 underestimates the average IWC, underestimates Ni below $-60^{\circ}C$, and misses positive correlations between Di and Na_{100} .

5 Discussion and conclusions

In this study, we investigate the statistical distributions of cirrus cloud microphysical properties (i.e., IWC, Ni, and Di) as
well as several key controlling factors (i.e., temperature, RHi, σ_w and Na) using a comprehensive in situ observational
dataset and GCM simulations. Regional variations of cirrus cloud microphysical properties are examined for six latitudinal
300 regions in two hemispheres. Two types of CAM6 simulations are evaluated, i.e., nudged and free-running simulations.

Regarding the regional variations at warmer conditions (i.e., $-55^{\circ}C$ to $-40^{\circ}C$), the highest and lowest IWC values were
observed in NH midlatitude and SH midlatitude, respectively, while the polar regions show the lowest Ni and highest Di
(Figures 4 and 5). The hemispheric differences between NH and SH midlatitudes indicate a possible role of anthropogenic
aerosols in controlling ice microphysical properties. The tropical regions show the highest IWC and Ni at temperatures
305 below $-55^{\circ}C$ possibly due to convection anvils with the droplet freezing from down below or homogeneous nucleation in
gravity waves generated by convection. This feature is corroborated by the fact that tropical regions show the highest RHi
values for both clear-sky and in-cloud conditions (Figure 6), while the midlatitude and polar regions show fewer samples
exceeding the homogeneous nucleation threshold. The higher RHi values in tropics are likely contributed by higher updrafts
310 (indicated by higher σ_w in Figure 8). These results demonstrate the important roles of these controlling factors on cirrus
clouds at different latitudinal and temperature ranges.

Evaluating the model simulations of cirrus microphysical properties, different model performance results are seen in
different regions. For example, simulations underestimated the IWC and Ni in NH midlatitude (Figures 4 and 5), possibly
due to model dry bias to form ice clouds (as discussed in Wu et al. (2017)) and/or smaller aerosol indirect effects on IWC
and Ni in the simulations (Figure 13). For RHi distributions, the simulations represent a similar peak position at ice
315 saturation for in-cloud RHi PDFs compared with observations but underestimate the frequency and magnitude of ISS for
clear-sky condition. For σ_w distributions, simulations represent similar regional variations of σ_w compared with observations,
with σ_w decreasing from lower to higher latitudes. However, larger biases are seen in the simulations for the effects of RHi
and σ_w on ice microphysical properties, including the simulated average IWC and Ni maximize at 80% RHi instead of 110%
RHi as observed, and the simulation misses the increasing average Di with increasing σ_w as observed.

320 For aerosol indirect effects, the simulations underestimate IWC, Ni, Di as well as cloud fraction at colder conditions
($< -60^{\circ}C$) when larger aerosols exist, indicating that the effectiveness of larger aerosols is underestimated at the colder



conditions. The observations also show higher Di than simulations by a factor of 3 – 4 at warmer temperatures (-50°C to -40°C), indicating inefficient ice particle growth and/or sedimentation in the simulations. In addition, the observed IWC, Ni and Di show significant increase at higher Na_{500} ($>10\text{ cm}^{-3}$) and Na_{100} ($>100\text{ cm}^{-3}$), while simulations do not show such significant increase. This result indicates that aerosol indirect effects may be underestimated especially for higher Na values. Overall, the global-scale observational dataset used in this study provides statistically robust distributions of cirrus cloud microphysical properties, which can be used to evaluate the effects of thermodynamics, dynamics and aerosols on cirrus clouds in a global climate model. Extending from previous studies that investigated climate model sensitivity to individual cirrus cloud controlling factors, i.e., w (Shi and Liu, 2016), RHi (D'Alessandro et al., 2019), water vapor (Wu et al., 2017), and aerosols (Wang et al., 2014), this study provides a comprehensive analysis of all factors. In addition, further attention was given towards evaluating these factors in the simulations based on geographical locations. Even though small ice particles ($< 62.5\text{ }\mu\text{m}$) are excluded in this study, correlations between ice microphysical properties and these key controlling factors are still clearly seen in the observation dataset. This study underscores the importance of correctly representing the thermodynamic, dynamic and aerosol conditions in climate models at various regions, as well as accurately simulating their correlations with ice microphysical properties. Failing to do so may result in biases of cirrus cloud microphysical properties depending on different regions and temperatures, leading to biases in cirrus cloud radiative effects on a global scale.

Data Availability

Observations from the seven NSF flight campaigns are accessible at <https://data.eol.ucar.edu/>.

Author contributions

340 R. Patnaude and M. Diao contributed to the development of the ideas, conducted quality control to aircraft-based observations, and wrote the majority of the manuscript. R. Patnaude contributed to all model simulations and the subsequent data analysis. X. Liu and S. Chu provided expertise on the set-up of CAM6 model simulations and provided input to the analysis of simulation data.

Competing interests

345 The authors declare that they have no conflict of interest.

Acknowledgments

R. Patnaude and M. Diao acknowledge funding support from U. S. National Science Foundation grants AGS-1642291 and OPP-1744965. R. Patnaude also acknowledges support from the San Jose State University Walker Fellowship. For funding



support in 2016 and 2018 summer, M. Diao acknowledges the NCAR Advanced Study Program (ASP) Faculty Fellowship.
350 X. Liu and S. Chu acknowledge the support of the National Science Foundation under grant AGS-1642289. We would like to acknowledge the NCAR/Earth Observation Laboratory flight teams from the seven flight campaigns: START08, HIPPO, PREDICT, DC3, CONTRAST, TORERO, and ORCAS. For in situ observations of water vapor by the VCSEL hygrometer, field support, calibration and QA/QC was conducted by M. Diao, J. DiGangi, M. Zondlo, and S. Beaton. Additional appreciation is given to Jorgen Jensen, Chris Webster, and Christina McCluskey for helpful discussions.

355 References

Barth, M. C., Cantrell, C. A., Brune, W. H., Rutledge, S. A., Crawford, J. H., Huntrieser, H., Carey, L. D., MacGorman, D., Weisman, M., Pickering, K. E., Bruning, E., Anderson, B., Apel, E., Biggerstaff, M., Campos, T., Campuzano-Jost, P., Cohen, R., Crounse, J., Day, D. A., Diskin, G., Flocke, F., Fried, A., Garland, C., Heikes, B., Honomichl, S., Hornbrook, R., Gregory Huey, L., Jimenez, J. L., Lang, T., Lichtenstern, M., Mikoviny, T., Nault, B., O'Sullivan, D., Pan, L. L., Peischl, J., Pollack, I., Richter, D., Riemer, D., Ryerson, T., Schlager, H., St. Clair, J., Walega, J., Weibring, P., Weinheimer, A., Wennberg, P., Wisthaler, A., Wooldridge, P. J. and Ziegler, C.: The Deep Convective Clouds and Chemistry (DC3) field campaign, *Bull. Am. Meteorol. Soc.*, 96(8), 1281–1310, doi:10.1175/BAMS-D-13-00290.1, 2015.

Bogenschutz, P. A., Gettelman, A., Morrison, H., Larson, V. E., Craig, C. and Schanen, D. P.: Higher-order turbulence closure and its impact on climate simulations in the community atmosphere model, *J. Clim.*, 26(23), 9655–9676, doi:10.1175/JCLI-D-13-00075.1, 2013.

Boucher, O., Randall, D., Artaxo, P., Bretherton, C., Feingold, G., Forster, P., Kerminen, V.-M., Kondo, Y., Liao, H., Lohmann, U., Rasch, P., Satheesh, S. K., Sherwood, S. C., Stevens, B. and Zhang, X.-Y.: Clouds and aerosols, *Clim. Chang. 2013 Phys. Sci. Basis Work. Gr. I Contrib. to Fifth Assess. Rep. Intergov. Panel Clim. Chang.*, 9781107057(July), 571–658, doi:10.1017/CBO9781107415324.016, 2013.

Brown, P. R. A. and Francis, P. N.: Improved Measurements of the Ice Water Content in Cirrus Using a Total-Water Probe, *J. Atmos. Ocean. Technol.*, 12, 410–414, doi:10.1175/1520-0426(1995)012%3C0410:IMOTIW%3E2.0.CO;2, 1995.

Chylek, P., Dubey, M. K., Lohmann, U., Ramanathan, V., Kaufman, Y. J., Lesins, G., Hudson, J., Altmann, G. and Olsen, S.: Aerosol indirect effect over the Indian Ocean, *Geophys. Res. Lett.*, 33(6), L06806, doi:10.1029/2005GL025397, 2006.

Cziczo, D. J. and Froyd, K. D.: Sampling the composition of cirrus ice residuals, *Atmos. Res.*, 142, 15–31, doi:10.1016/j.atmosres.2013.06.012, 2014.

Cziczo, D. J., Froyd, K. D., Hoose, C., Jensen, E. J., Diao, M., Zondlo, M. A., Smith, J. B., Twohy, C. H. and Murphy, D. M.: Clarifying the dominant sources and mechanisms of cirrus cloud formation, *Science* (80-..), 340(6138), 1320–1324, doi:10.1126/science.1234145, 2013.



D'Alessandro, J. J., Diao, M., Wu, C., Liu, X., Chen, M., Morrison, H., Eidhammer, T., Jensen, J. B., Bansemer, A., Zondlo, M. A. and DiGangi, J. P.: Dynamical conditions of ice supersaturation and ice nucleation in convective systems: A comparative analysis between in situ aircraft observations and WRF simulations, *J. Geophys. Res.*, 122(5), 2844–2866, doi:10.1002/2016JD025994, 2017.

385 D'Alessandro, J. J., Diao, M., Wu, C., Liu, X., Jensen, J. B. and Stephens, B. B.: Cloud phase and relative humidity distributions over the Southern Ocean in austral summer based on in situ observations and CAM5 simulations, *J. Clim.*, 32(10), 2781–2805, doi:10.1175/JCLI-D-18-0232.1, 2019.

DeMott, P. J., Prenni, A. J., Liu, X., Kreidenweis, S. M., Petters, M. D., Twohy, C. H., Richardson, M. S., Eidhammer, T. and Rogers, D. C.: Predicting global atmospheric ice nuclei distributions and their impacts on climate, *Proc. Natl. Acad. Sci.*, 107(25), 11217–11222, doi:10.1073/pnas.0910818107, 2010.

390 Diao, M., Zondlo, M. A., Heymsfield, A. J., Beaton, S. P. and Rogers, D. C.: Evolution of ice crystal regions on the microscale based on in situ observations, *Geophys. Res. Lett.*, 40(13), 3473–3478, doi:10.1002/grl.50665, 2013.

Diao, M., Zondlo, M. A., Heymsfield, A. J., Avallone, L. M., Paige, M. E., Beaton, S. P., Campos, T. and Rogers, D. C.: Cloud-scale ice-supersaturated regions spatially correlate with high water vapor heterogeneities, *Atmos. Chem. Phys.*, 14(5), 2639–2656, doi:10.5194/acp-14-2639-2014, 2014a.

395 Diao, M., Zondlo, M. A., Heymsfield, A. J. and Beaton, S. P.: Hemispheric comparison of cirrus cloud evolution using in situ measurements in HIAPER Pole-to-Pole Observations, *Geophys. Res. Lett.*, 41(11), 1–8, doi:10.1002/2014GL059873, 2014b.

Diao, M., Jensen, J. B., Pan, L. L., Homeyer, C. R., Honomichl, S., Bresch, J. F. and Bansemer, A.: Distributions of ice 400 supersaturation and ice crystals from airborne observations in relation to upper tropospheric dynamical boundaries, *J. Geophys. Res.*, 120(10), 5101–5121, doi:10.1002/2015JD023139, 2015.

Diao, M., Bryan, G. H., Morrison, H. and Jensen, J. B.: Ice nucleation parameterization and relative humidity distribution in idealized squall-line simulations, *J. Atmos. Sci.*, 74(9), 2761–2787, doi:10.1175/JAS-D-16-0356.1, 2017.

Eidhammer, T., Morrison, H., Bansemer, A., Gettelman, A. and Heymsfield, A. J.: Comparison of ice cloud properties 405 simulated by the Community Atmosphere Model (CAM5) with in-situ observations, *Atmos. Chem. Phys.*, 14(18), 10103–10118, doi:10.5194/acp-14-10103-2014, 2014.

Eidhammer, T., Morrison, H., Mitchell, D., Gettelman, A. and Erfani, E.: Improvements in global climate model 410 microphysics using a consistent representation of ice particle properties, *J. Clim.*, 30(2), 609–629, doi:10.1175/JCLI-D-16-0050.1, 2017.

Gelaro, R., McCarty, W., Suárez, M. J., Todling, R., Molod, A., Takacs, L., Randles, C. A., Darmenov, A., Bosilovich, M. G., Reichle, R., Wargan, K., Coy, L., Cullather, R., Draper, C., Akella, S., Buchard, V., Conaty, A., da Silva, A. M., Gu, W., Kim, G. K., Koster, R., Lucchesi, R., Merkova, D., Nielsen, J. E., Partyka, G., Pawson, S., Putman, W., Rienecker, M., Schubert, S. D., Sienkiewicz, M. and Zhao, B.: The modern-era retrospective analysis for research and applications, version 2 (MERRA-2), *J. Clim.*, 30(14), 5419–5454, doi:10.1175/JCLI-D-16-0758.1, 2017.



415 Gettelman, A. and Morrison, H.: Advanced two-moment bulk microphysics for global models. Part I: Off-line tests and
comparison with other schemes, *J. Clim.*, 28(3), 1268–1287, doi:10.1175/JCLI-D-14-00102.1, 2015.

Gettelman, A., Liu, X., Ghan, S. J., Morrison, H., Park, S., Conley, A. J., Klein, S. A., Boyle, J., Mitchell, D. L. and Li, J. L.
F.: Global simulations of ice nucleation and ice supersaturation with an improved cloud scheme in the Community
Atmosphere Model, *J. Geophys. Res. Atmos.*, 115(18), 1–19, doi:10.1029/2009JD013797, 2010.

420 Golaz, J. C., Larson, V. E. and Cotton, W. R.: A PDF-Based Model for Boundary Layer Clouds. Part I : Method and Model
Description, *J. Atmos. Sci.*, 59, 3540–3551, 2002.

Heymsfield, A. J., Krämer, M., Wood, N. B., Gettelman, A., Field, P. R. and Liu, G.: Dependence of the Ice Water Content
and Snowfall Rate on Temperature, Globally: Comparison of in Situ Observations, Satellite Active Remote Sensing
Retrievals, and Global Climate Model Simulations, *J. Appl. Meteorol. Climatol.*, 56(190), 189–215, doi:10.1175/JAMC-
425 D-16-0230.1, 2017.

Jensen, E. J., Toon, O. B., Vay, S. A., Ovarlez, J., May, R., Bui, T. P., Twohy, C. H., Gandrud, B. W., Pueschel, R. F. and
Schumann, U.: Prevalence of ice-supersaturated regions in the upper troposphere: Implications for optically thin ice
cloud formation, *J. Geophys. Res. Atmos.*, 106(D15), 17253–17266, doi:10.1029/2000JD900526, 2001.

430 Kanitz, T., Seifert, P., Ansmann, A., Engelmann, R., Althausen, D., Casiccia, C. and Rohwer, E. G.: Contrasting the impact
of aerosols at northern and southern midlatitudes on heterogeneous ice formation, *Geophys. Res. Lett.*, 38(17), 1–5,
doi:10.1029/2011GL048532, 2011.

Kärcher, B. and Lohmann, U.: A parameterization of cirrus cloud formation: Homogeneous freezing of supercooled aerosols,
J. Geophys. Res., 107(D2), doi:10.1029/2001JD000470, 2002.

Kärcher, B. and Lohmann, U.: A parameterization of cirrus cloud formation: Heterogeneous freezing, *J. Geophys. Res.*,
435 107(D14), 4402, doi:10.1029/2002JD003220, 2003.

Kärcher, B., Hendricks, J. and Lohmann, U.: Physically based parameterization of cirrus cloud formation for use in global
atmospheric models, *J. Geophys. Res. Atmos.*, 111, D01205, doi:10.1029/2005JD006219, 2006.

Koop, T., Luo, B., Tsias, A. and Peter, T.: Water activity as the determinant for homogeneous ice nucleation in aqueous
solutions, *Nature*, 406(6796), 611–614, doi:10.1038/35020537, 2000.

440 Kooperman, G. J., Pritchard, M. S., Ghan, S. J., Wang, M., Somerville, R. C. J. and Russell, L. M.: Constraining the
influence of natural variability to improve estimates of global aerosol indirect effects in a nudged version of the
Community Atmosphere Model 5, *J. Geophys. Res. Atmos.*, 117(23), 1–16, doi:10.1029/2012JD018588, 2012.

Krämer, M., Schiller, C., Afchine, A., Bauer, R., Gensch, I., Mangold, A., Schlicht, S., Spelten, N., Sitnikov, N., Borrmann,
S., De Reus, M. and Spichtinger, P.: Ice supersaturations and cirrus cloud crystal numbers, *Atmos. Chem. Phys.*, 9(11),
445 3505–3522, doi:10.5194/acp-9-3505-2009, 2009.

Krämer, M., Rolf, C., Luebke, A., Afchine, A., Spelten, N., Costa, A., Meyer, J., Zöger, M., Smith, J., Herman, R. L.,
Buchholz, B., Ebert, V., Baumgardner, D., Borrmann, S., Klingebiel, M. and Avallone, L.: A microphysics guide to
cirrus clouds – Part 1: Cirrus types, *Atmos. Chem. Phys.*, 16(5), 3463–3483, doi:10.5194/acp-16-3463-2016, 2016.



Krämer, M., Rolf, C., Spelten, N., Afchine, A., Fahey, D., Jensen, E., Khaykin, S., Kuhn, T., Lawson, P., Lykov, A., Pan, L.
450 L., Riese, M., Rollins, A., Stroh, F., Thornberry, T., Wolf, V., Woods, S., Spichtinger, P., Quaas, J. and Sourdeval, O.: A Microphysics Guide to Cirrus – Part II : Climatologies of Clouds and Humidity from Observations, *Atmos. Chem. Phys. Discuss.*, (January), 2020.

Kuebbeler, M., Lohmann, U., Hendricks, J. and Kärcher, B.: Dust ice nuclei effects on cirrus clouds, *Atmos. Chem. Phys.*, 14(6), 3027–3046, doi:10.5194/acp-14-3027-2014, 2014.

455 Lin, S. J.: A “vertically Lagrangian” finite-volume dynamical core for global models, *Mon. Weather Rev.*, 132(10), 2293–2307, doi:10.1175/1520-0493(2004)132<2293:AVLFDC>2.0.CO;2, 2004.

Liu, X. and Penner, J. E.: Ice nucleation parameterization for global models, *Meteorol. Zeitschrift*, 14(4), 499–514, doi:10.1127/0941-2948/2005/0059, 2005.

460 Liu, X., Penner, J. E., Ghan, S. J. and Wang, M.: Inclusion of ice microphysics in the NCAR Community Atmospheric Model version 3 (CAM3), *J. Clim.*, 20(18), 4526–4547, doi:10.1175/JCLI4264.1, 2007.

Liu, X., Shi, X., Zhang, K., Jensen, E. J., Gettelman, A., Barahona, D., Nenes, A. and Lawson, P.: Sensitivity studies of dust ice nuclei effect on cirrus clouds with the community atmosphere model CAM5, *Atmos. Chem. Phys.*, 12(24), 12061–12079, doi:10.5194/acp-12-12061-2012, 2012.

465 Liu, X., Ma, P. L., Wang, H., Tilmes, S., Singh, B., Easter, R. C., Ghan, S. J. and Rasch, P. J.: Description and evaluation of a new four-mode version of the Modal Aerosol Module (MAM4) within version 5.3 of the Community Atmosphere Model, *Geosci. Model Dev.*, 9(2), 505–522, doi:10.5194/gmd-9-505-2016, 2016.

Luebke, A. E., Avallone, L. M., Schiller, C., Meyer, J., Rolf, C. and Krämer, M.: Ice water content of Arctic, midlatitude, and tropical cirrus - Part 2: Extension of the database and new statistical analysis, *Atmos. Chem. Phys.*, 13(13), 6447–6459, doi:10.5194/acp-13-6447-2013, 2013.

470 Luebke, A. E., Afchine, A., Costa, A., Groß, J. U., Meyer, J., Rolf, C., Spelten, N., M Avallone, L., Baumgardner, D. and Krämer, M.: The origin of midlatitude ice clouds and the resulting influence on their microphysical properties, *Atmos. Chem. Phys.*, 16(9), 5793–5809, doi:10.5194/acp-16-5793-2016, 2016.

Mace, G. G. and Wrenn, F. J.: Evaluation of the hydrometeor layers in the East and West Pacific within ISCCP cloud-top pressure-optical depth bins using merged CloudSat and CALIPSO data, *J. Clim.*, 26(23), 9429–9444, doi:10.1175/JCLI-D-12-00207.1, 2013.

475 Minikin, A., Petzold, A., Ström, J., Krejci, R., Seifert, M., van Velthoven, P., Schlager, H. and Schumann, U.: Aircraft observations of the upper tropospheric fine particle aerosol in the Northern and Southern Hemispheres at midlatitudes, *Geophys. Res. Lett.*, 30(10), doi:10.1029/2002gl016458, 2003.

Montgomery, M. T., Davis, C., Dunkerton, T., Wang, Z., Velden, C., Torn, R., Majumdar, S. J., Zhang, F., Smith, R. K.,
480 Bosart, L., Bell, M. M., Haase, J. S., Heymsfield, A., Jensen, J., Campos, T. and Boothe, M. A.: The pre-depression investigation of cloud-systems in the tropics (PREDICT) experiment: Scientific basis, new analysis tools, and some first results, *Bull. Am. Meteorol. Soc.*, 93(2), 153–172, doi:10.1175/BAMS-D-11-00046.1, 2012.



Muhlbauer, A., Ackerman, T. P., Comstock, J. M., Diskin, G. S., Evans, S. M., Lawson, R. P. and Marchand, R. T.: Impact of large-scale dynamics on the microphysical properties of midlatitude cirrus, *J. Geophys. Res.*, 119(7), 3976–3996, 485 doi:10.1002/2013JD020035, 2014a.

Muhlbauer, A., Kalesse, H. and Kollas, P.: Vertical velocities and turbulence in midlatitude anvil cirrus: A comparison between in situ aircraft measurements and ground-based Doppler cloud radar retrievals, *Geophys. Res. Lett.*, 41(22), 7814–7821, doi:10.1002/2014GL062279, 2014b.

Murphy, D. M. and Koop, T.: Review of the vapour pressures of ice and supercooled water for atmospheric applications, *Q. J. R. Meteorol. Soc.*, 131(608), 1539–1565, doi:10.1256/qj.04.94, 2005. 490

Pan, L. L., Bowman, K. P., Atlas, E. L., Wofsy, S. C., Zhang, F., Bresch, J. F., Ridley, B. A., Pittman, J. V., Homeyer, C. R., Romashkin, P. and Cooper, W. A.: The stratosphere-troposphere analyses of regional transport 2008 experiment, *Bull. Am. Meteorol. Soc.*, 91(3), 327–342, doi:10.1175/2009BAMS2865.1, 2010.

Pan, L. L., Atlas, E. L., Salawitch, R. J., Honomichl, S. B., Bresch, J. F., Randel, W. J., Apel, E. C., Hornbrook, R. S., 495 Weinheimer, A. J., Anderson, D. C., Andrews, S. J., Baidar, S., Beaton, S. P., Campos, T. L., Carpenter, L. J., Chen, D., Dix, B., Donets, V., Hall, S. R., Hanisco, T. F., Homeyer, C. R., Huey, L. G., Jensen, J. B., Kaser, L., Kinnison, D. E., Koenig, T. K., Lamarque, J.-F., Liu, C., Luo, J., Luo, Z. J., Montzka, D. D., Nicely, J. M., Pierce, R. B., Riemer, D. D., Robinson, T., Romashkin, P., Saiz-Lopez, A., Schauffler, S., Shieh, O., Stell, M. H., Ullmann, K., Vaughan, G., Volkamer, R. and Wolfe, G.: The Convective Transport of Active Species in the Tropics (CONTRAST) Experiment, 500 *Bull. Am. Meteorol. Soc.*, 98(1), 106–128, doi:10.1175/bams-d-14-00272.1, 2017.

Patnaude, R. and Diao, M.: Aerosol indirect effects on cirrus clouds based on global aircraft observations, *Geophys. Res. Lett.*, 47, doi:10.1029/2019gl086550, 2020.

Penner, J. E., Chen, Y., Wang, M. and Liu, X.: Possible influence of anthropogenic aerosols on cirrus clouds and anthropogenic forcing, *Atmos. Chem. Phys.*, 9(3), 879–896, doi:10.5194/acp-9-879-2009, 2009.

505 Penner, J. E., Zhou, C., Garnier, A. and Mitchell, D. L.: Anthropogenic Aerosol Indirect Effects in Cirrus Clouds, *J. Geophys. Res. Atmos.*, 123(20), 11,652-11,677, doi:10.1029/2018JD029204, 2018.

Prenni, A. J., Petters, M. D., Faulhaber, A., Carriço, C. M., Ziemann, P. J., Kreidenweis, S. M. and DeMott, P. J.: Heterogeneous ice nucleation measurements of secondary organic aerosol generated from ozonolysis of alkenes, *Geophys. Res. Lett.*, 36(6), 1–5, doi:10.1029/2008GL036957, 2009.

510 Righi, M., Hendricks, J., Lohmann, U., Gerhard Beer, C., Hahn, V., Heinold, B., Heller, R., Krämer, M., Ponater, M., Rolf, C., Tegen, I. and Voigt, C.: Coupling aerosols to (cirrus) clouds in the global EMAC-MADE3 aerosol-climate model, *Geosci. Model Dev.*, 13(3), 1635–1661, doi:10.5194/gmd-13-1635-2020, 2020.

Sassen, K., Wang, Z. and Liu, D.: Global distribution of cirrus clouds from CloudSat/cloud-aerosol lidar and infrared pathfinder satellite observations (CALIPSO) measurements, *J. Geophys. Res. Atmos.*, 113(8), 1–12, 515 doi:10.1029/2008JD009972, 2008.

Schiller, C., Krämer, M., Afchine, A., Spelten, N. and Sitnikov, N.: Ice water content of Arctic, midlatitude, and tropical



cirrus, *J. Geophys. Res. Atmos.*, 113(D24), 1–12, doi:10.1029/2008JD010342, 2008.

Shi, X. and Liu, X.: Effect of cloud-scale vertical velocity on the contribution of homogeneous nucleation to cirrus formation and radiative forcing, *Geophys. Res. Lett.*, 43(12), 6588–6595, doi:10.1002/2016GL069531, 2016.

520 Shi, X., Liu, X. and Zhang, K.: Effects of pre-existing ice crystals on cirrus clouds and comparison between different ice nucleation parameterizations with the Community Atmosphere Model (CAM5), *Atmos. Chem. Phys.*, 15, 1503–1520, doi:10.5194/acp-15-1503-2015, 2015.

Stephens, B. B., Long, M. C., Keeling, R. F., Kort, E. A., Sweeney, C., Apel, E. C., Atlas, E. L., Beaton, S., Bent, J. D., Blake, N. J., Bresch, J. F., Casey, J., Daube, B. C., Diao, M., Diaz, E., Dierssen, H., Donets, V., Gao, B.-C., Gierach, 525 M., Green, R., Haag, J., Hayman, M., Hills, A. J., Hoecker-Martínez, M. S., Honomichl, S. B., Hornbrook, R. S., Jensen, J. B., Li, R.-R., McCubbin, I., McKain, K., Morgan, E. J., Nolte, S., Powers, J. G., Rainwater, B., Randolph, K., Reeves, M., Schauffler, S. M., Smith, K., Smith, M., Stith, J., Stossmeister, G., Toohey, D. W. and Watt, A. S.: The O₂/N₂ Ratio and CO₂ Airborne Southern Ocean Study, *Bull. Am. Meteorol. Soc.*, 99(2), 381–402, doi:10.1175/BAMS-D-16-0206.1, 2018.

530 Stephens, G. and Webster, P.: Clouds and climate: Sensitivity of simple systems, *J. Atmos. Sci.*, 38, 235–247, 1981.

Storelvmo, T. and Herger, N.: Cirrus cloud susceptibility to the injection of ice nuclei in the upper troposphere, *J. Geophys. Res.*, 119(5), 2375–2389, doi:10.1002/2013JD020816, 2014.

Tan, X., Huang, Y., Diao, M., Bansemer, A., Zondlo, M. A., DiGangi, J. P., Volkamer, R. and Hu, Y.: An assessment of the 535 radiative effects of ice supersaturation based on in situ observations, *Geophys. Res. Lett.*, 43(20), 11,039–11,047, doi:10.1002/2016GL071144, 2016.

Volkamer, R., Baidar, S., Campos, T. L., Coburn, S., DiGangi, J. P., Dix, B., Eloranta, E. W., Koenig, T. K., Morley, B., Ortega, I., Pierce, B. R., Reeves, M., Sinreich, R., Wang, S., Zondlo, M. A. and Romashkin, P. A.: Aircraft 540 measurements of BrO, IO, glyoxal, NO₂, H₂O, O₂-O₂ and aerosol extinction profiles in the tropics: Comparison with aircraft-/ship-based in situ and lidar measurements, *Atmos. Meas. Tech.*, 8(5), 2121–2148, doi:10.5194/amt-8-2121-2015, 2015.

Wang, M. and Penner, J. E.: Cirrus clouds in a global climate model with a statistical cirrus cloud scheme, *Atmos. Chem. Phys.*, 10(12), 5449–5474, doi:10.5194/acp-10-5449-2010, 2010.

Wang, M., Liu, X., Zhang, K. and Comstock, J. M.: Aerosol effects on cirrus through ice nucleation in the Community 545 Atmosphere Model CAM5 with a statistical cirrus scheme, *J. Adv. Model. Earth Syst.*, 6, 513–526, doi:10.1002/2014MS000339, 2014.

Wofsy, S. C.: HIAPER Pole-to-Pole Observations (HIPPO): Fine-grained, global-scale measurements of climatically important atmospheric gases and aerosols, *Philos. Trans. R. Soc. A Math. Phys. Eng. Sci.*, 369(1943), 2073–2086, doi:10.1098/rsta.2010.0313, 2011.

Wolf, V., Kuhn, T., Milz, M., Voelger, P., Krämer, M. and Rolf, C.: Arctic ice clouds over northern Sweden: Microphysical 550 properties studied with the Balloon-borne Ice Cloud particle Imager B-ICI, *Atmos. Chem. Phys.*, 18(23), 17371–17386,



doi:10.5194/acp-18-17371-2018, 2018.

Wu, C., Liu, X., Diao, M., Zhang, K., Gettelman, A., Lu, Z., Penner, J. E. and Lin, Z.: Direct comparisons of ice cloud macro- and microphysical properties simulated by the Community Atmosphere Model version 5 with HIPPO aircraft observations, *Atmos. Chem. Phys.*, 17(7), 4731–4749, doi:10.5194/acp-17-4731-2017, 2017.

555 Zhang, G. J. and McFarlane, N. A.: Sensitivity of climate simulations to the parameterization of cumulus convection in the
canadian climate centre general circulation model, *Atmos. - Ocean*, 33(3), 407–446,
doi:10.1080/07055900.1995.9649539, 1995.

Zhang, K., Liu, X., Wang, M., Comstock, J. M., Mitchell, D. L., Mishra, S. and Mace, G. G.: Evaluating and constraining ice
cloud parameterizations in CAM5 using aircraft measurements from the SPARTICUS campaign, *Atmos. Chem. Phys.*,
560 13(9), 4963–4982, doi:10.5194/acp-13-4963-2013, 2013.

Zhang, Y., MacKe, A. and Albers, F.: Effect of crystal size spectrum and crystal shape on stratiform cirrus radiative forcing,
Atmos. Res., 52(1–2), 59–75, doi:10.1016/S0169-8095(99)00026-5, 1999.

Zhao, B., Liou, K.-N., Gu, Y., Jiang, J. H., Li, Q., Fu, R., Huang, L., Liu, X., Shi, X., Su, H. and He, C.: Impact of aerosols
on ice crystal size, *Atmos. Chem. Phys.*, 18, 1065–1078, doi:10.5194/acp-18-1065-2018, 2018.

565 Zhao, B., Wang, Y., Gu, Y., Liou, K. N., Jiang, J. H., Fan, J., Liu, X., Huang, L. and Yung, Y. L.: Ice nucleation by aerosols
from anthropogenic pollution, *Nat. Geosci.*, doi:10.1038/s41561-019-0389-4, 2019.

Zhou, C., Penner, J., Lin, G., Liu, X. and Wang, M.: What controls the low ice number concentration in the upper
troposphere?, *Atmos. Chem. Phys.*, 16(19), 12411–12424, doi:10.5194/acp-16-12411-2016, 2016.

Zondlo, M. A., Paige, M. E., Massick, S. M. and Silver, J. A.: Vertical cavity laser hygrometer for the National Science
570 Foundation Gulfstream-V aircraft, *J. Geophys. Res. Atmos.*, 115(20), 1–14, doi:10.1029/2010JD014445, 2010.



Table 1. Descriptions of seven NSF flight campaigns conducted with the NSF/NCAR G-V research aircraft.

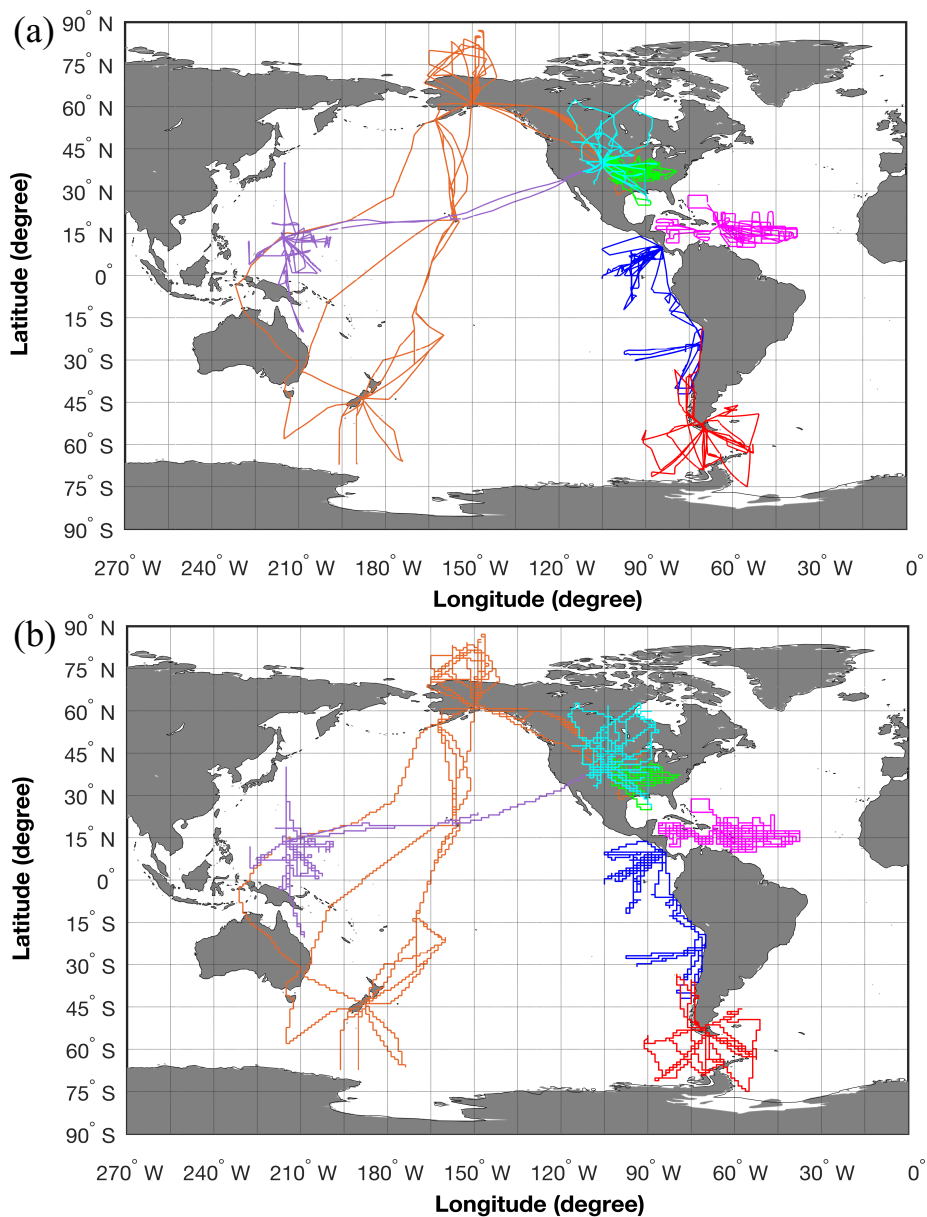
Acronym	Field Campaign	Time	Lat, Lon	Region*	Flight hours	In-cloud hours	Clear-sky hours
START08	Stratosphere-Troposphere Analyses of Regional Transport	April – June 2008	26°N – 62°N, 117°W – 86°W	NM, NP	84	2	52
HIPPO	HIAPER Pole-to-pole Observations deployments 2 – 5	Oct – Nov 2009; Mar – Apr 2010; Jun – July 2011; Aug – Sept 2011	87°N – 67°S, 128°E – 90°W	A	333	7	111
PREDICT	PRE-Depression Investigation of Cloud Systems in the Tropics	Aug – Sept 2010	10°N – 28.5°N, 86°W – 37°W	NT	105	25	66
DC3	Deep Convective Clouds and Chemistry Project	May – June 2012	25°N – 42°N, 106°W – 80°W	NM	144	23	54
TORERO	Tropical Ocean tRoposphere Exchange of Reactive halogen species and Oxygenated voc	Jan – Feb 2012	42°S – 14°N, 105°W – 70°W	NT, ST, SM	125	2	52
CONTRAST	CONvective TRansport of Active Species in the Tropics	Jan – Feb 2014	20°S – 40°N, 132°E – 105°W	NM, NT, ST	116	23	48
ORCAS	The O ₂ /N ₂ Ratio and CO ₂ Airborne Southern Ocean (ORCAS) Study	Jan – Mar 2016	75°S – 18°S, 91°W – 51°W	SM, SP	95	1	40

575 *: N, northern hemisphere; S, southern hemisphere; T, tropics; M, midlatitude; P, polar regions; A, all regions.



Table 2. Ranges of meteorological conditions and ice microphysical properties for in situ observations, CAM6-nudg and CAM6-free data used in this study.

	In situ observations	CAM6-nudg	CAM6-free
T (°C)	-78 – -40	-75 – -40	-89.9 – -40
P (Pa)	12,389 – 53,137	12,300 – 53,446	12,300 – 53,100
RHi (%)	0.3 – 175.1	0.0473 – 159.8	0.002 – 257.19
IWC (g/m ³)	0.00004 – 23.31	0.00001 – 32.65	0.00001 – 94.72
Ni (#/L)	0.039 – 542.15	0.01 – 5,238	0.0243 – 6,066
Di (μm)	62.5 – 3,200	62.5 – 1,958	66.7 – 2,556



START08, HIPPO, PREDICT, TORERO, DC3, CONTRAST, ORCAS

580 **Figure 1.** Global maps of flight tracks representing the seven campaigns in this study for (a) in situ observations and (b)
CAM6-nudg. Colors denote different campaigns.

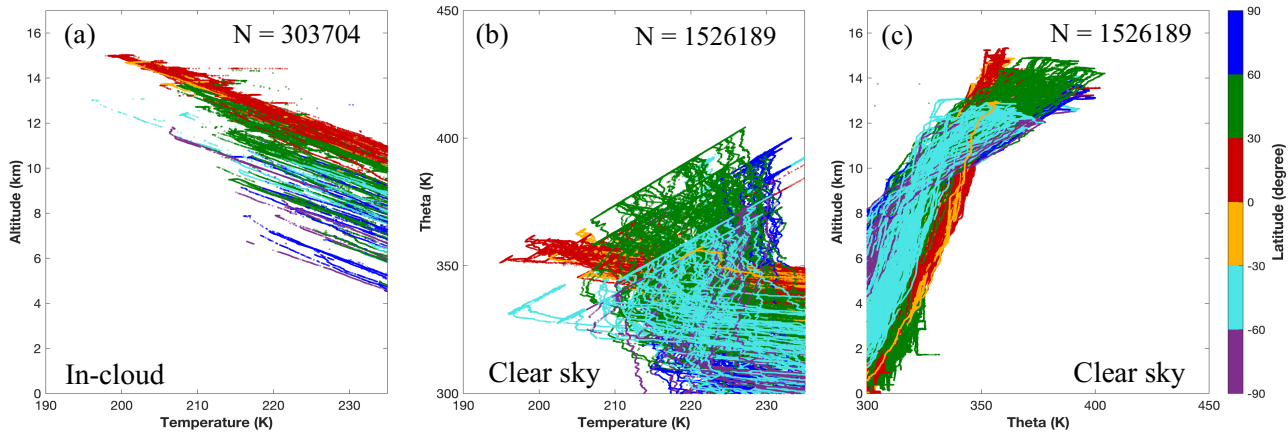


Figure 2. (a) Vertical profiles of temperature, (b) potential temperature vs. temperature, and (c) vertical profiles of potential temperature based on in situ observations at temperatures $\leq -40^{\circ}\text{C}$. Number of samples (N) for 1-Hz observations is shown in the figure legend. Colors denote six latitudinal regions.

585

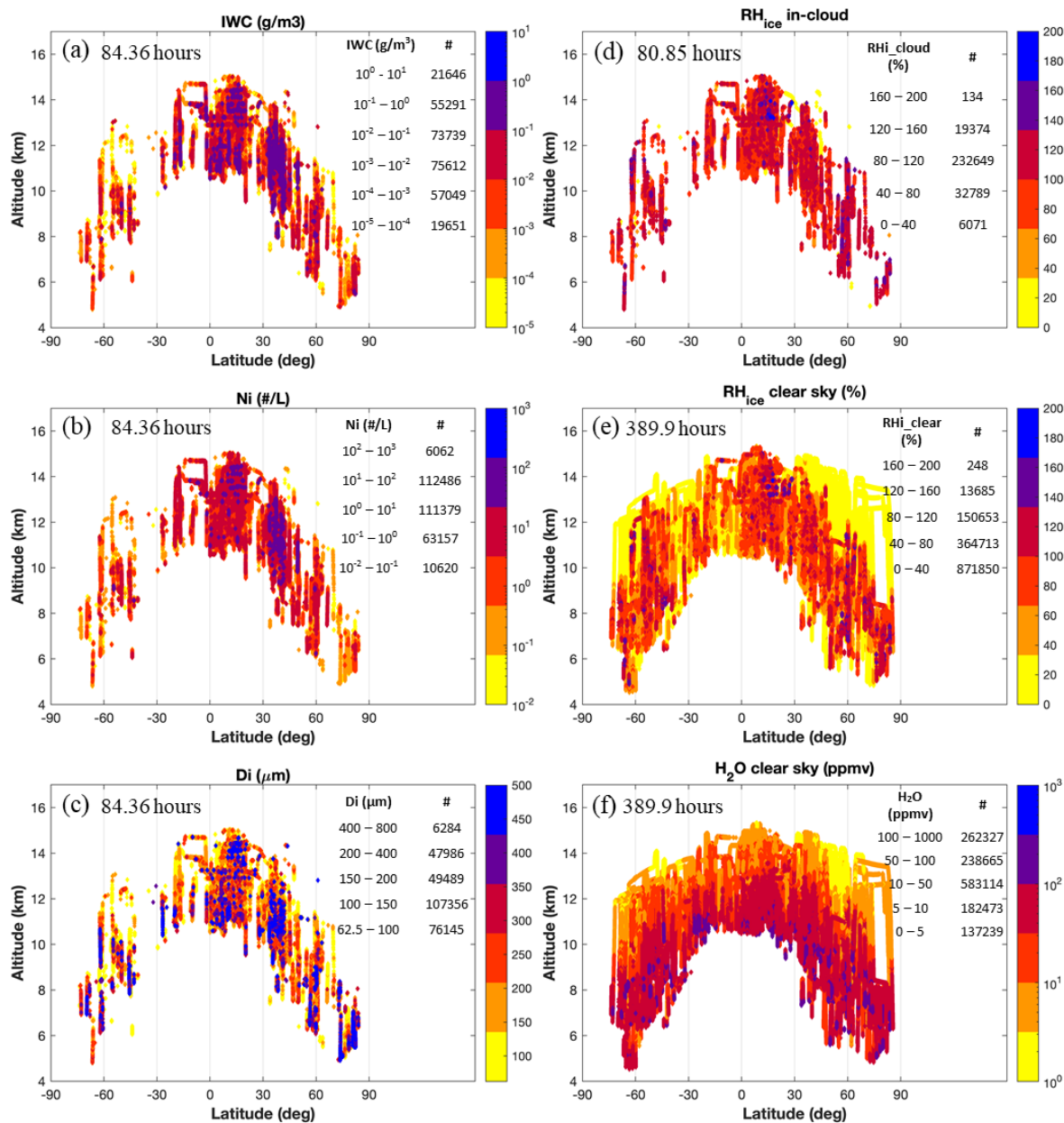


Figure 3. Latitude and altitude distributions of (a) IWC, (b) Ni, (c) Di, (d) in-cloud RH_i, (e) clear-sky RH_i, and (f) clear-sky water vapor volume mixing ratio at temperatures $\leq -40^{\circ}\text{C}$. Total measurement hours and number of samples for given intervals are shown for each variable. Note that the measurement ranges shown in the upper right corner are not the full ranges (see Table 2 for the full ranges).

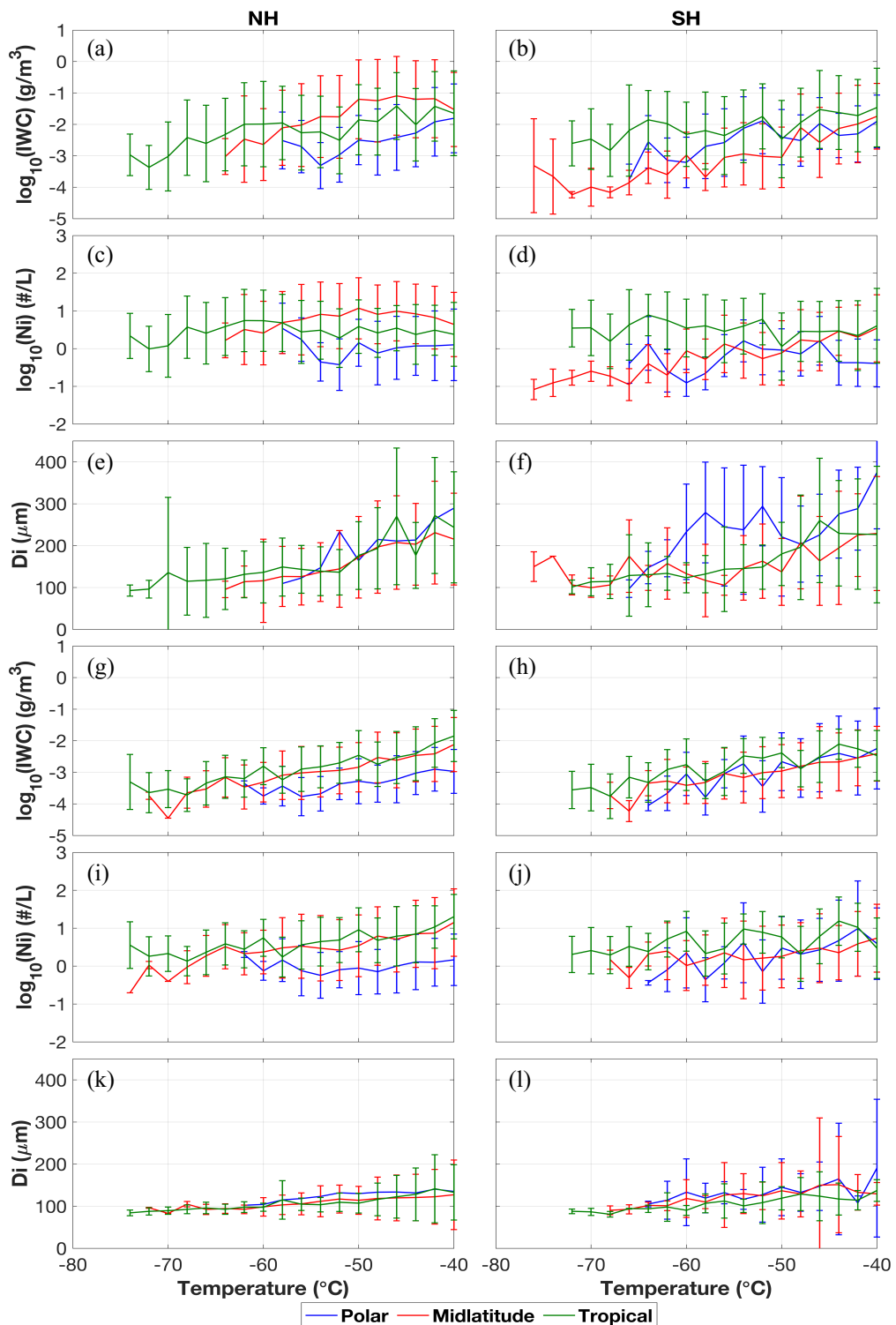




Figure 4. Geometric means of (a, b, g and h) IWC and (c, d, i and j) Ni, as well as (e, f, k and l) linear averages of Di at 4 °C temperature intervals between -80 °C and -40 °C, compared between in situ observations (first three rows) and CAM6-nudg (bottom three rows). Whiskers represent \pm one standard deviation. The number of samples for 1-Hz observations at 595 temperatures $\leq -40^{\circ}\text{C}$ in the northern (southern) hemisphere tropical, midlatitude and polar regions are 173930 (15569), 100615 (3809), and 6704 (2606), respectively. The number of samples for CAM6-nudg data in these regions are 2992408 (595392), 2082130 (617007) and 523430 (212686), respectively.

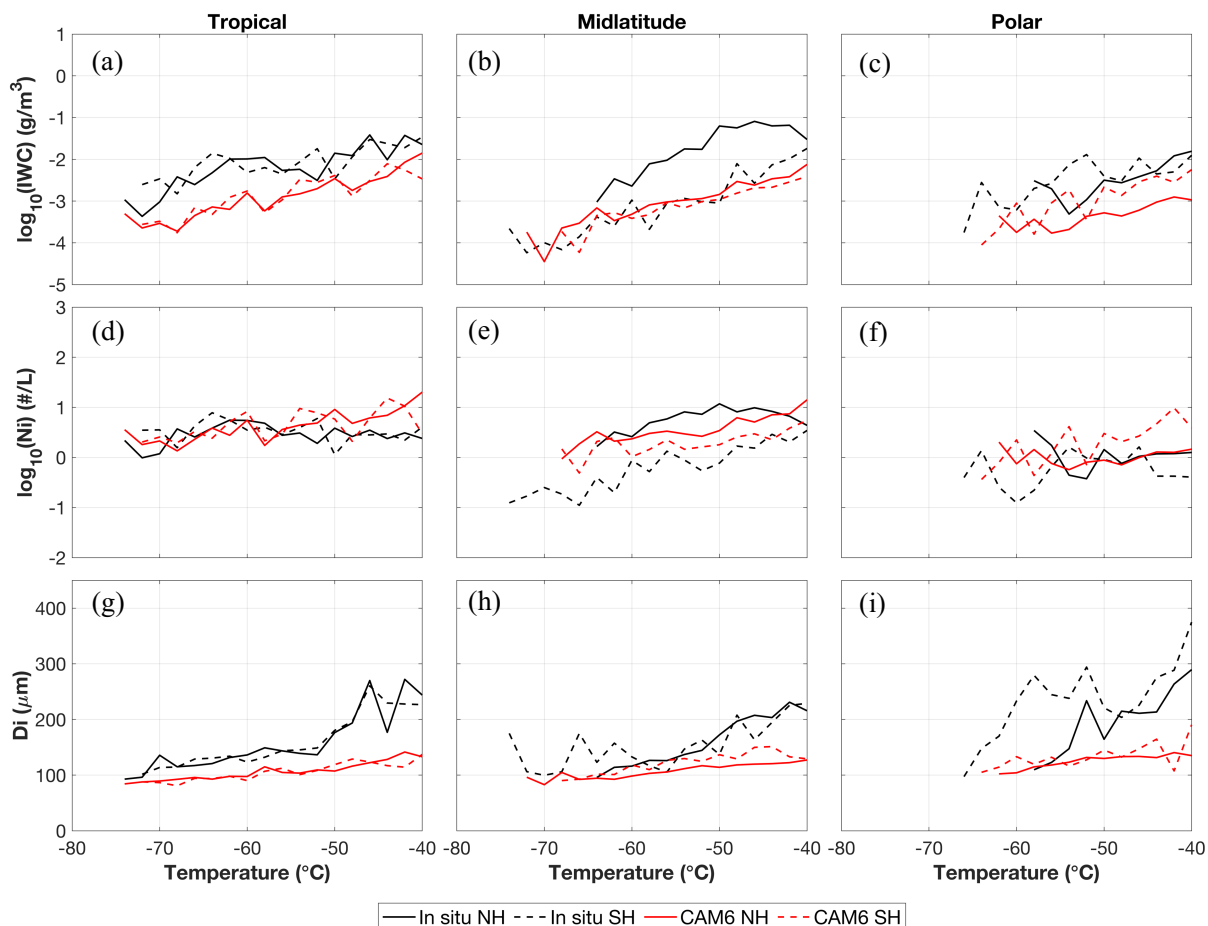
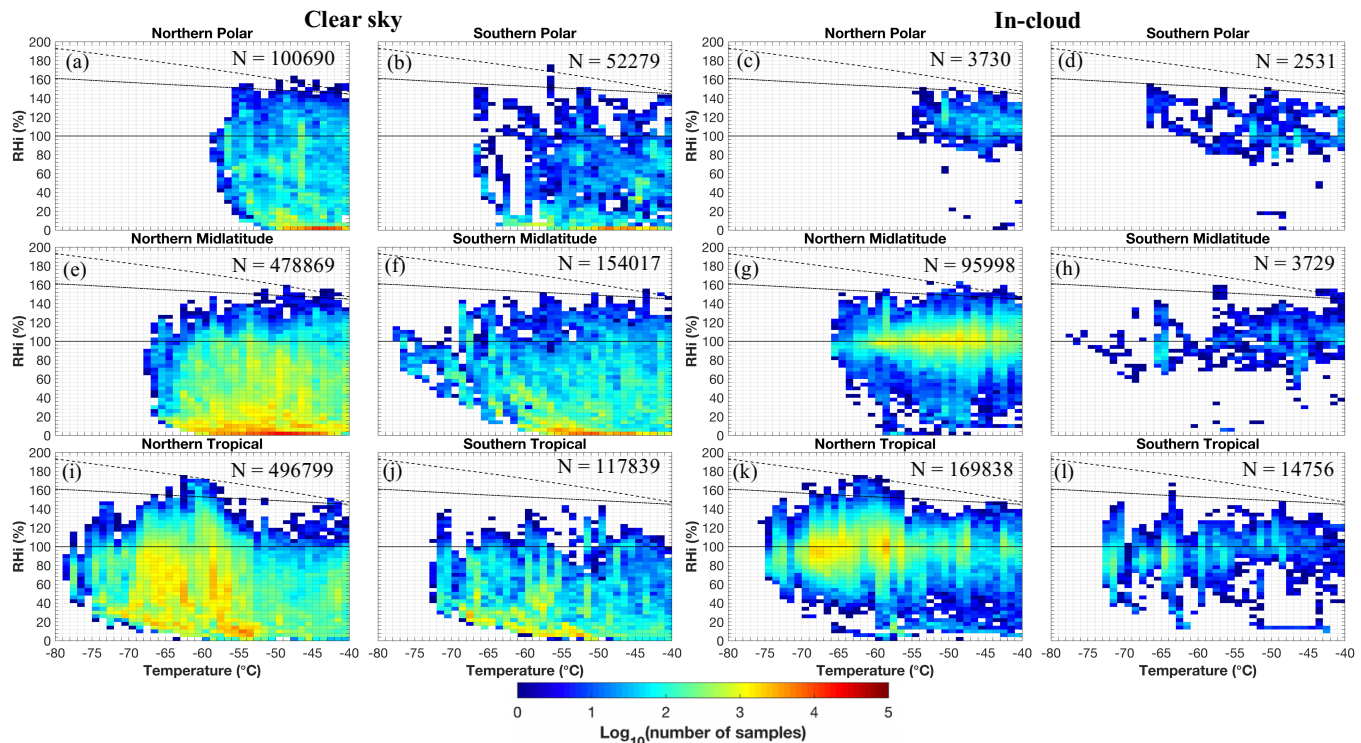
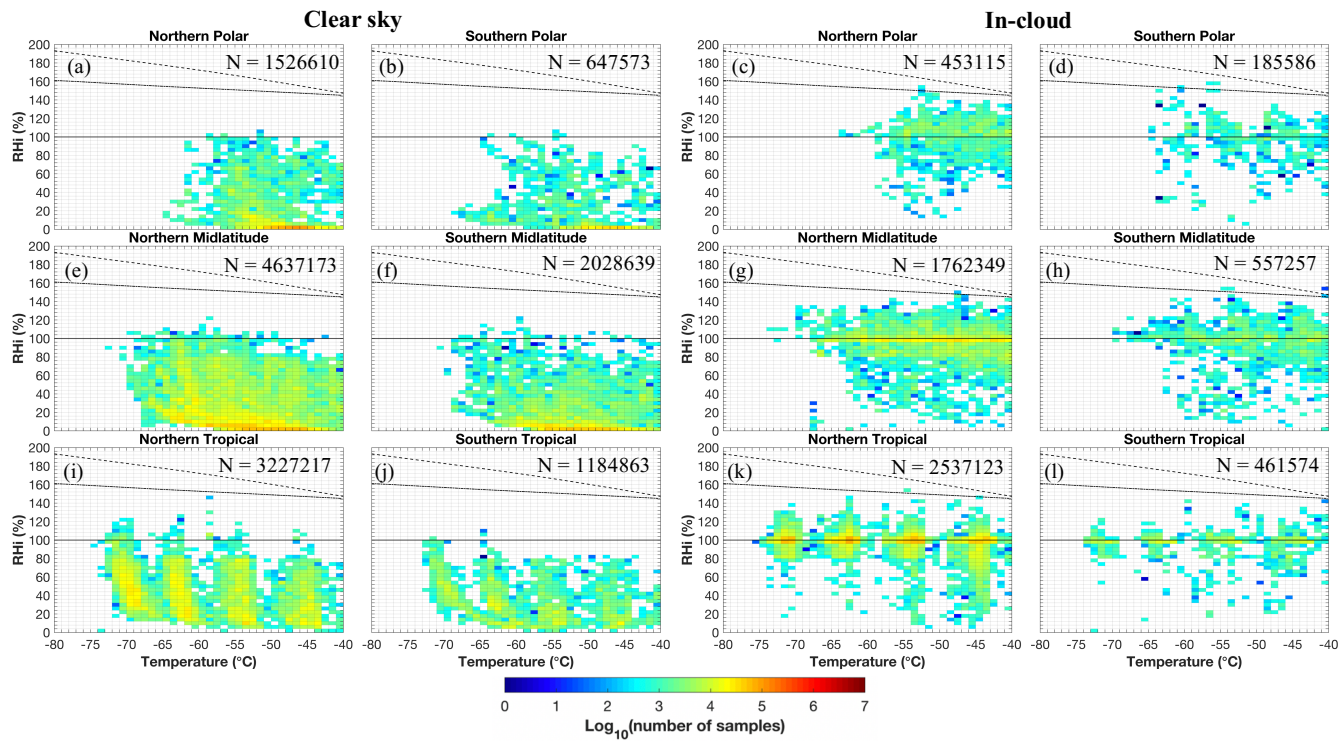


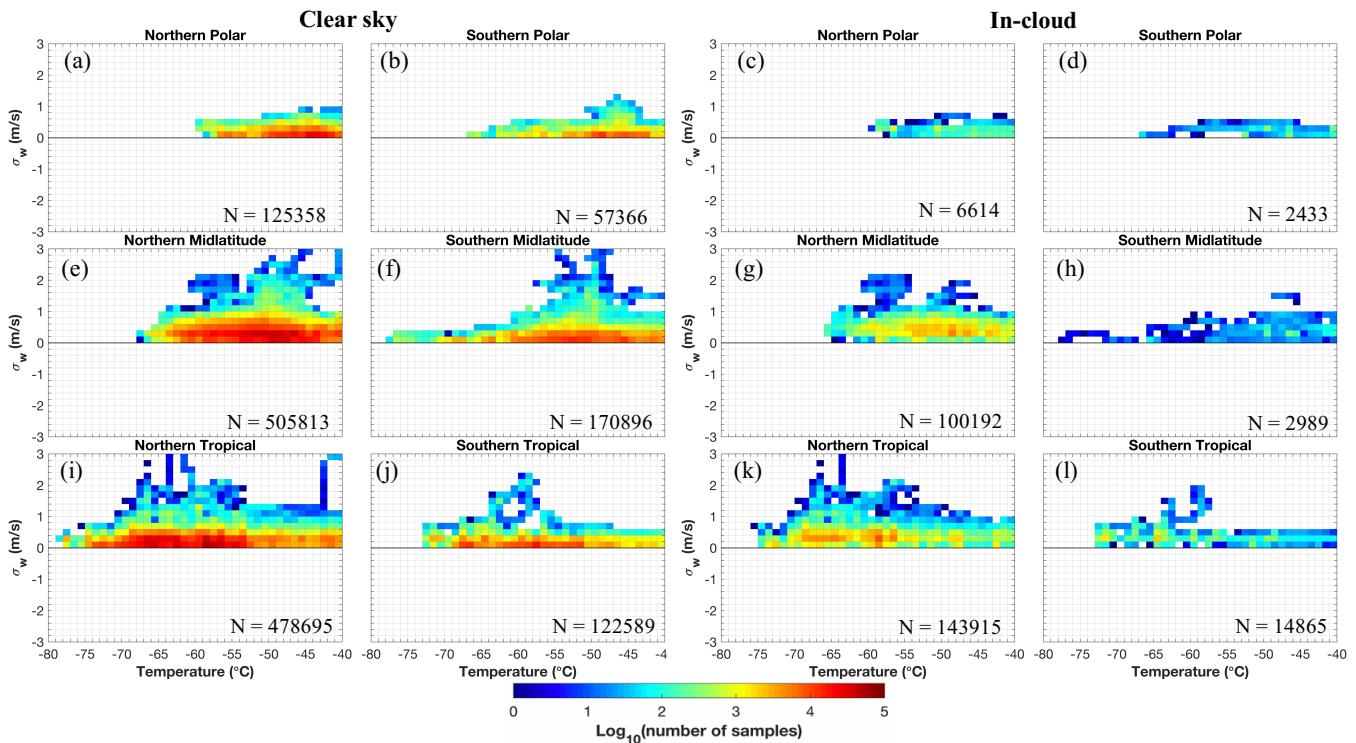
Figure 5. Geometric means of (a – c) IWC and (d – f) Ni, as well as (g – i) linear averages of Di at 4 $^{\circ}\text{C}$ temperature intervals between -80 $^{\circ}\text{C}$ and -40 $^{\circ}\text{C}$, compared between in situ observations (black lines) and CAM6-nudg (red lines). Observed and simulated microphysical properties are binned by six latitudinal regions similar to Figure 4, where NH is denoted by solid lines, and SH is denoted by dashed lines. Number of samples in this figure is the same as those shown in Figure 4 caption.



605 **Figure 6.** Distributions of RH at various temperatures and geographical locations from in situ observations under (left two columns) clear-sky and (right two columns) in-cloud conditions. Solid and dashed black lines represent ice and liquid
 606 saturation, calculated based on saturation vapor pressure with respect to ice and liquid from Murphy and Koop (2005),
 607 respectively. Dash-dotted line denotes the homogeneous freezing threshold for 0.5 μm aerosols based on Koop et al. (2000).



610 **Figure 7.** Similar to Figure 6 but for CAM6-nudg data. RH values for simulations are calculated using simulated specific
humidity and temperature, based on the equation of saturation vapor pressure with respect to ice from Murphy and Koop
(2005).



615 **Figure 8.** Distributions of σ_w at various temperatures and geographical locations from in situ observations under (left two columns) clear-sky and (right two columns) in-cloud conditions.

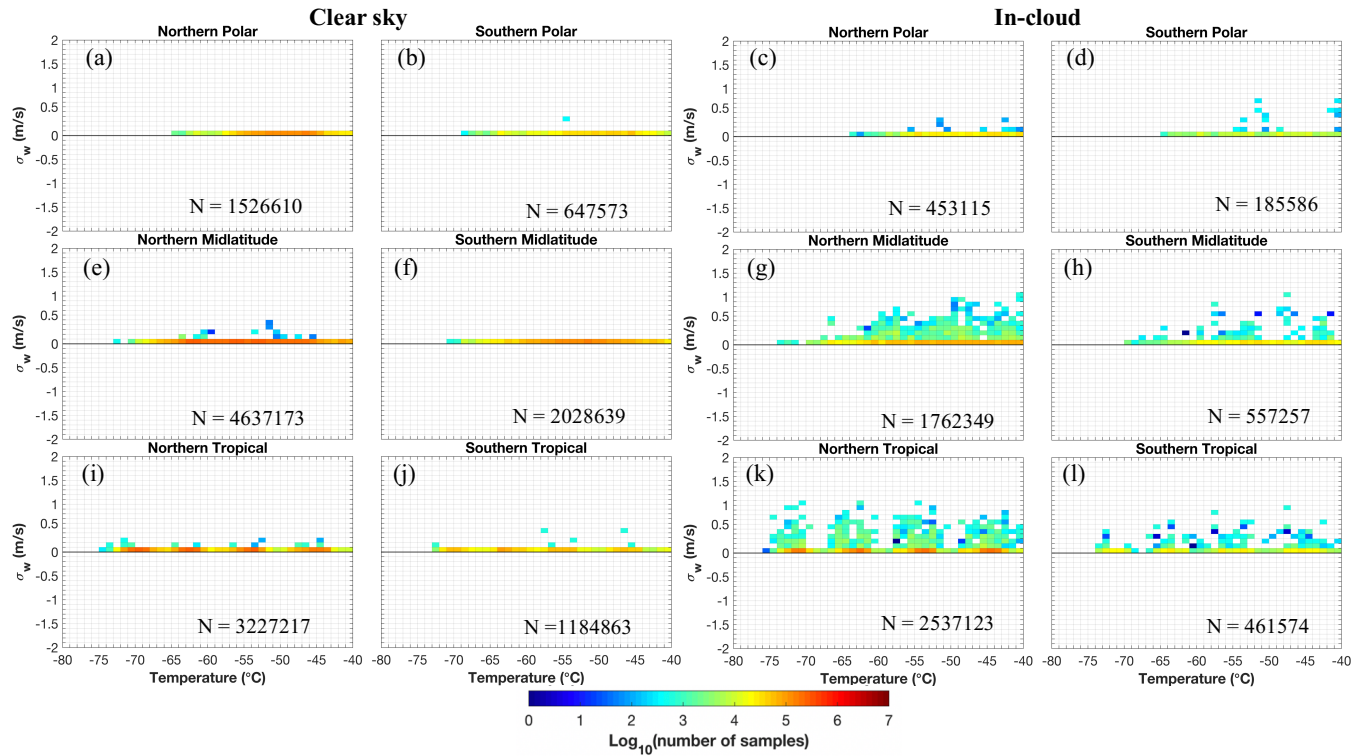
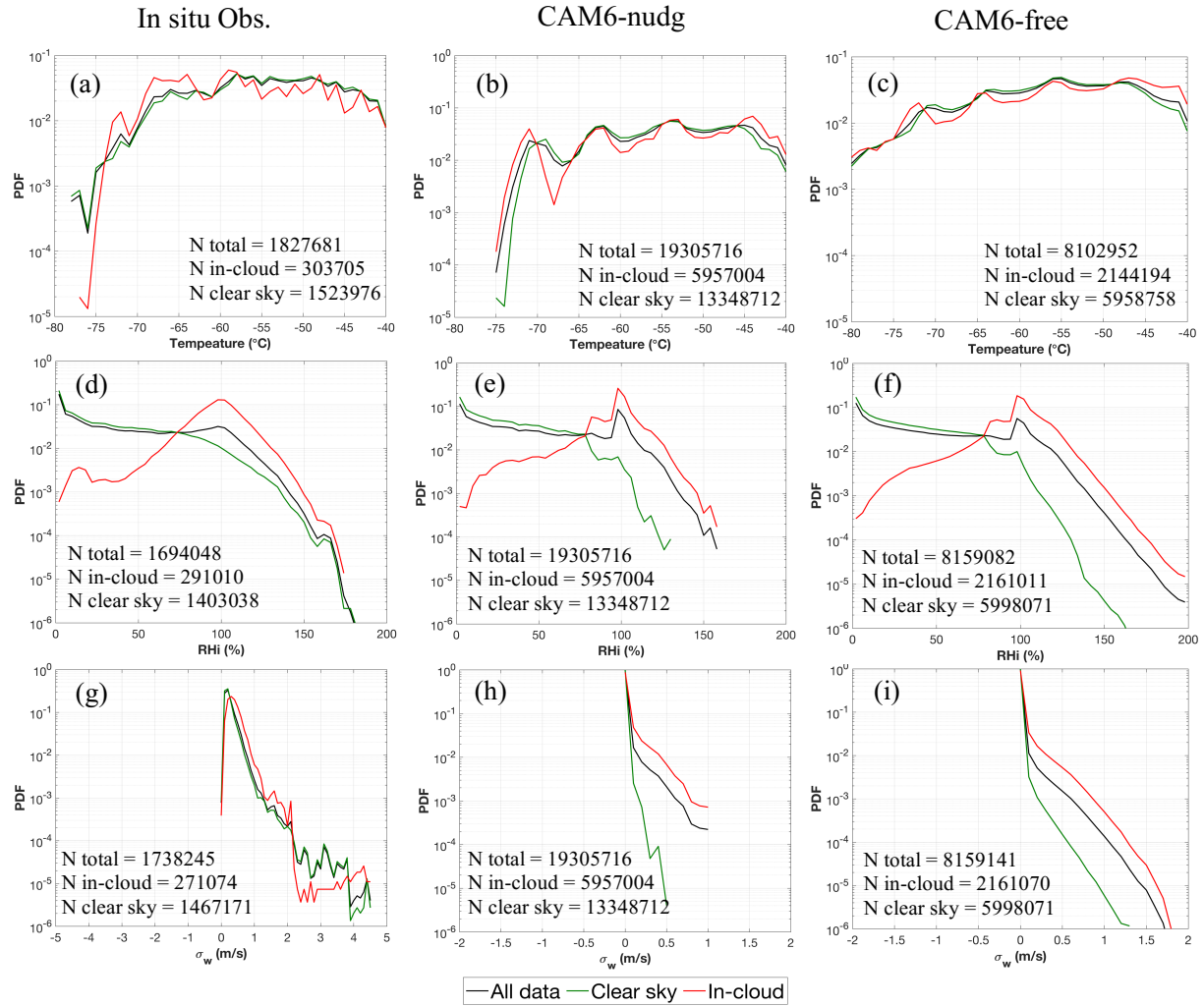


Figure 9. Similar to Figure 8 but for the CAM6-nudg data.



620 **Figure 10.** Probability density functions (PDFs) for (a – c) temperature, (d – f) RHi and (g – i) σ_w , compared among (left column) observations, (middle column) CAM6-nudg and (right column) CAM6-free data.

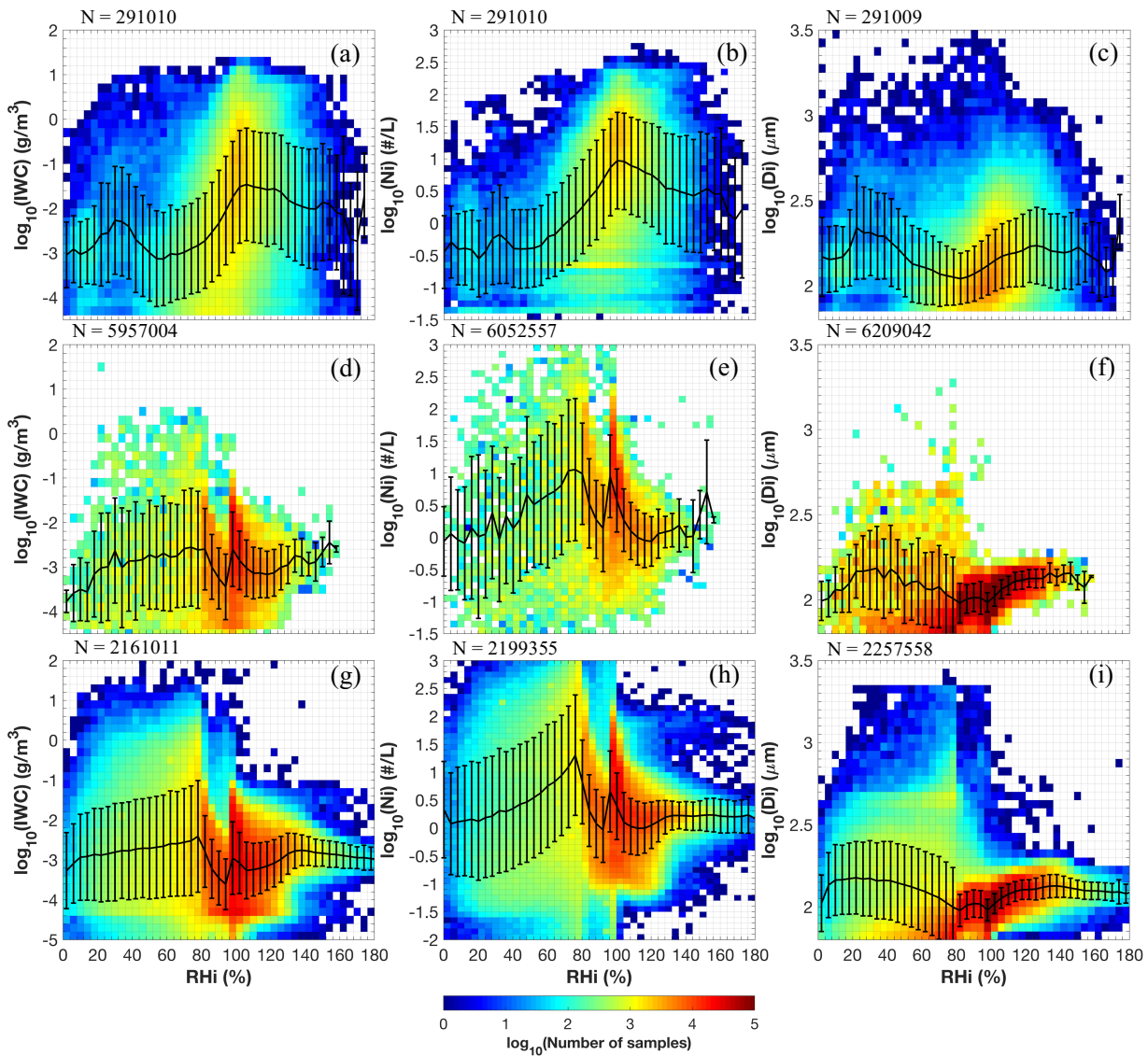


Figure 11. Correlations between RHi and in-cloud IWC, Ni and Di (columns 1 – 3, respectively), compared among (a – c) in situ observations, (d – f) CAM6-nudg, and (g – i) CAM6-free data. Black lines and whiskers denote geometric means and standard deviations, respectively.

625

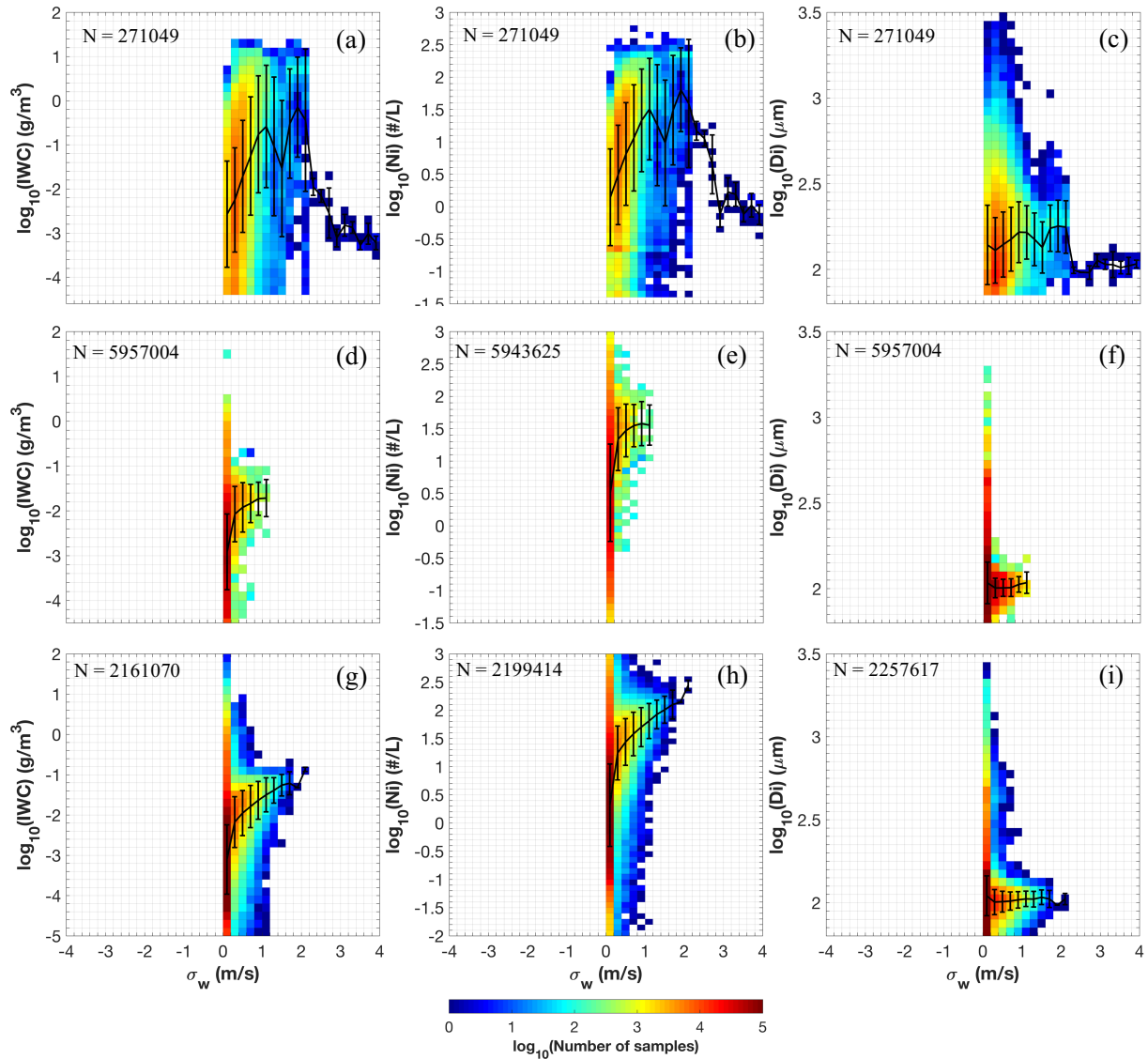


Figure 12. Similar to Figure 11 but for correlations with σ_w .

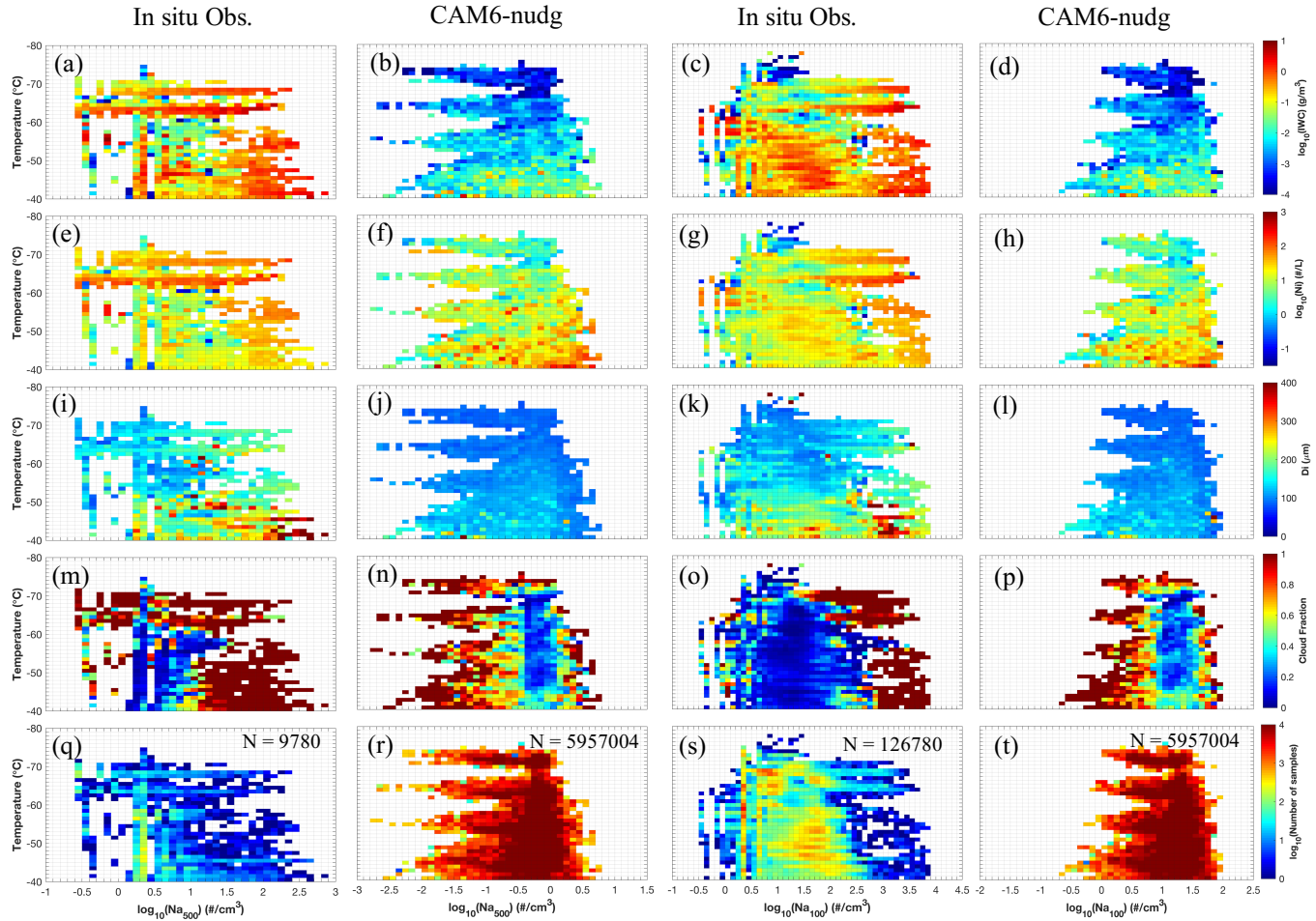


Figure 13. Aerosol indirect effects on (a – d) IWC, (e – h) Ni, (i – l) Di, and (m – p) cloud fraction, compared between 630 observations and CAM6-nudg data, examined for (left two columns) $\log_{10}(Na_{500})$ and (right two columns) $\log_{10}(Na_{100})$. Number of samples is shown in the bottom row. Cloud fraction is calculated as the number of in-cloud samples over the total number of samples for a given temperature and Na bin.